ARTICLES
https://doi.org/10.1038/s41564-021-00894-z
nature microbiology

Check for updates

Cell division in the archaeon *Haloferax volcanii* relies on two FtsZ proteins with distinct functions in division ring assembly and constriction

Yan Liao[1,3], Solenne Ithurbide[1,3], Christian Evenhuis[1], Jan Löwe[2] and Iain G. Duggin[1]✉

In bacteria, the tubulin homologue FtsZ assembles a cytokinetic ring, termed the Z ring, and plays a key role in the machinery that constricts to divide the cells. Many archaea encode two FtsZ proteins from distinct families, FtsZ1 and FtsZ2, with previously unclear functions. Here, we show that *Haloferax volcanii* cannot divide properly without either or both FtsZ proteins, but DNA replication continues and cells proliferate in alternative ways, such as blebbing and fragmentation, via remarkable envelope plasticity. FtsZ1 and FtsZ2 colocalize to form the dynamic division ring. However, FtsZ1 can assemble rings independent of FtsZ2, and stabilizes FtsZ2 in the ring, whereas FtsZ2 functions primarily in the constriction mechanism. FtsZ1 also influenced cell shape, suggesting it forms a hub-like platform at midcell for the assembly of shape-related systems too. Both FtsZ1 and FtsZ2 are widespread in archaea with a single S-layer envelope, but archaea with a pseudomurein wall and division septum only have FtsZ1. FtsZ1 is therefore likely to provide a fundamental recruitment role in diverse archaea, and FtsZ2 is required for constriction of a flexible S-layer envelope, where an internal constriction force might dominate the division mechanism, in contrast with the single-FtsZ bacteria and archaea that divide primarily by wall ingrowth.

FtsZ is the most conserved bacterial cell division protein and among the first molecules to assemble at the incipient division site. It forms a dynamic ring-like structure around the cell that acts as a platform to initiate the recruitment of about a dozen core components and up to ~30 other factors involved in division[1,2]. Within the ring, FtsZ polymerizes dynamically in a GTP-dependent manner near the inner surface of the cytoplasmic membrane, directing the inward synthesis of septal cell wall peptidoglycan to drive cell constriction, and may also provide a direct influence on membrane constriction[3–7]. The septal wall splits to separate the two new cells in a process that is either continuous with septal wall synthesis and ring closure or is activated after the septal cross-wall is complete[8,9].

An *ftsZ* homologue was first identified in several archaea by DNA hybridization[10,11] and GTP-binding screens[12]. Archaeal FtsZ showed GTPase activity in vitro[11] and was localized to the midcell by immunofluorescence[11,13]. In bacteria such as *Escherichia coli*, the actin homologue FtsA forms filaments that, together with ZipA and several regulatory or stabilization proteins, link FtsZ filaments to the inner membrane[2,14]. However, homologues of these and most other bacterial (and eukaryotic) cell division proteins appear to be largely absent in archaea. One exception and probable candidate is the archaeal homologue of SepF, which can polymerize and participates with FtsA in anchoring FtsZ for Gram-positive bacterial division[15], and shows strong phylogenetic association with FtsZ in archaea[16].

The first complete archaeal genome sequence, of *Methanocaldococcus jannaschii*[17], revealed multiple *ftsZ* homologues, whereas almost all bacterial genomes contain only one *ftsZ* required for division. Some archaea do not contain FtsZ, including the phylum Crenarchaeota, in which division is instead orchestrated by proteins related to the ESCRT-III complexes involved in membrane remodelling in eukaryotes[18,19]. Many of the archaea that contain FtsZ also have one or more tubulin superfamily protein from the CetZ family[20,21]. The genome of the archaeal model organism *Haloferax volcanii*[22] encodes eight tubulin superfamily proteins: six CetZs and two FtsZs. Work in *H. volcanii* showed that the CetZs were not individually required for division, but at least one is required for rod cell shape development[20]. In the same study, an FtsZ1–green fluorescent protein (GFP) fusion protein was observed to localize at the midcell. The results also suggested *H. volcanii* as an excellent model for archaeal cell biology, as it has relatively large and flat cells that show a variety of regulated morphologies and are well suited to light and electron microscopy[20,23,24]. Here, we use *H. volcanii* to demonstrate that FtsZ1 and FtsZ2 have different functions in the mechanism of archaeal cell division.

Results

Characteristics of two FtsZ families in archaea. We performed a molecular phylogenetic analysis of 149 tubulin superfamily proteins identified in 60 diverse archaeal genomes. Archaeal FtsZ1, FtsZ2 and the well-studied bacterial/plant FtsZ form three distinct families that are approximately equally divergent from one another (Extended Data Fig. 1a). The majority of archaea encoded both an FtsZ1 homologue and an FtsZ2 homologue, including most Euryarchaeota (for example, Halobacteria, Thermococci and Archaeoglobi) and the DPANN and Asgard superphyla (Supplementary Table 3). Interestingly, methanogenic Euryarchaeota, which characteristically have a pseudomurein wall not found in other species, were found to only possess FtsZ1 (Extended Data Fig. 1 and Supplementary Table 3). The Crenarchaeota and Thaumarchaeota lacked specific members of the FtsZ families, although other TACK superphylum organisms (for example, Bathyarchaeota) contained at least one (FtsZ2).

We noticed conserved differences between archaeal FtsZ1 and FtsZ2 that are primarily in the vicinity of the GTPase active site and longitudinal subunit interface in polymers (see Extended Data Fig. 1c–e and Supplementary Information). Conserved motifs were also identified in the amino (N)- and carboxy (C)-terminal tails that

[1]The iThree Institute, University of Technology Sydney, Sydney, New South Wales, Australia. [2]MRC Laboratory of Molecular Biology, Cambridge, UK. [3]These authors contributed equally: Yan Liao, Solenne Ithurbide. ✉e-mail: Iain.Duggin@uts.edu.au

differed from bacterial/plant FtsZ. These differences are likely to manifest as fundamental functional characteristics of the three FtsZ families but await further detailed investigations.

Depletion of FtsZ1 or FtsZ2 causes division defects in *H. volcanii*. Given that *ftsZ* genes are nearly ubiquitous and important for survival in bacteria[25], we first engineered *H. volcanii* strains in which expression of the genomic copy of the *ftsZ1* (HVO_0717) or *ftsZ2* (HVO_0581) gene was placed under the control of the highly specific tryptophan (Trp)-regulated promoter *p.tna*[26] (Supplementary Fig. 1); expression of each *ftsZ* could be maintained during strain construction and growth by the inclusion of Trp in the growth medium, or depleted by placing the cells into medium without Trp. The two corresponding strains grew well in the presence of 2 mM Trp and appeared of approximately normal size and shape (Fig. 1a; 0 h; leftmost panels). However, resuspension of growing cells in liquid medium without Trp caused a large increase in cell size over the 24-h sampling period (biomass doubling times of ~4.4 h over the first 9 h of log growth), as shown by phase-contrast microscopy (Fig. 1a) and Coulter cytometry cell volume distributions (Supplementary Fig. 2). This is morphologically analogous to the classical bacterial filamentous phenotype[27], and signifies a defect in the regulation or mechanism of cell division in both the *ftsZ1* and *ftsZ2* depletion strains. The *ftsZ2* depletion resulted in a stronger division defect (substantially larger cells) compared with the *ftsZ1* depletion (Fig. 1a and Supplementary Fig. 2). Western blotting showed that the cellular amount of FtsZ1 had decreased substantially by ~6–9 h after withdrawal of Trp from the *p.tna–ftsZ1* strain, whereas in the *p.tna–ftsZ2* strain, FtsZ2, had almost completely disappeared after 3 h (Fig. 1b). Whether the cell size difference is due to the different rates of depletion or differing roles and importance of the two FtsZ proteins to cell division is addressed further below.

Time-lapse microscopy of growing cells showed some FtsZ1-depleted cells dividing, apparently inefficiently, whereas FtsZ2 depletion appeared to strongly block division (for example, Fig. 1c). After the onset of depletion, some *p.tna–ftsZ2* cells initially developed a constriction but were unable to complete division; the partial constriction then reversed with further cell growth, but had a lingering influence on cell shape (Extended Data Fig. 2). Later in depletion, budding-like processes were observed that resulted in apparent vesicles or minicells of variable sizes (Supplementary Video 1; *p.tna–ftsZ2*). In some of the enlarged FtsZ1-depleted cells, a small cell fragment appeared at one side of the division plane during cell separation (Fig. 1c; arrow). In others, it appeared to be carved out from a cell edge (Supplementary Video 2). In contrast, FtsZ2-depleted cells were not seen actively dividing, although some showed blebbing from cellular lobes in these very large misshapen cells (Supplementary Video 3).

When FtsZ-depleted cells were resupplied with Trp at the commencement of time-lapse imaging (FtsZ restoration), the giant cells then became capable of dividing (Fig. 1d and Supplementary Video 1). Some underwent multiple simultaneous divisions, generating large cells that then underwent further division events to eventually re-establish a population of normal-sized cells. It was also clear that the division process itself was sometimes asymmetric (unilateral), where cell constriction occurs from only one edge (or predominately from one edge), and the plane of division was sometimes noticeably acentral or not straight nor perpendicular to the cell envelope (Supplementary Video 1). Irregular positioning of division sites may be expected based on the sensitivity of division site positioning mechanisms to cell size and shape[28], and this resulted in noticeable pleomorphology in the progeny.

DNA composition of *H. volcanii* cells depleted of FtsZ1 or FtsZ2. To assess the positioning and replication of DNA in cells after depletion of each FtsZ, we stained the cells with SYTOX Green (SG) DNA stain. The giant cells showed DNA–SG staining that appeared diffusely present throughout the cytoplasm, similar to the staining intensity and distribution in wild-type cells (Extended Data Fig. 3a). Flow cytometry showed that DNA–SG fluorescence correlated with the side-scatter signal as a proxy for cell size (Extended Data Fig. 3b). Some of the largest mutant cells (for example, after *ftsZ2* depletion) showed ~100-fold higher DNA–SG fluorescence and side scatter than wild-type cells, corresponding to an expected genome copy number of ~2,000 or more in the largest mutant cells, compared with the typical polyploidy of ~20 in unmodified *H. volcanii*[29]. These results indicate that DNA synthesis continues in approximate proportion to cell biomass increase during inhibition of cell division caused by FtsZ depletion, and are consistent with the previously observed simple correlation between DNA content and cell size in wild-type *H. volcanii*[30] that reflects an absence of distinct cell cycle phases (Extended Data Fig. 3b).

***H. volcanii* propagates without FtsZ1 and/or FtsZ2.** The *p.tna–ftsZ1* and *p.tna–ftsZ2* strains were grown continuously at a range of Trp concentrations (from 0–2 mM Trp) and showed an inverse relationship between Trp concentration and cell size (Supplementary Fig. 3a,b). Since both *ftsZ* depletion strains could be maintained indefinitely in standard growth medium (Hv-Cab) in the absence of added Trp, we sought to determine whether the *ftsZ* genes were completely dispensable by employing a direct selection procedure to delete each gene. The Δ*ftsZ1* and Δ*ftsZ2* strains were viable. We also made a double deletion (Δ*ftsZ1* Δ*ftsZ2*), then confirmed the deletions by PCR and genome sequencing. Mid-log cultures had biomass doubling times of 3.08 ± 0.06 h (H26 wild type), 3.58 ± 0.27 h (Δ*ftsZ1*), 3.56 ± 0.23 h (Δ*ftsZ2*) and 4.20 ± 0.18 h (Δ*ftsZ1* Δ*ftsZ2*) (means ± 95% confidence intervals; Supplementary Fig. 4a). Dilution and agar plating of mid-log samples (optical density measured at a wavelength of 600 nm (OD_{600}) = 0.2) showed that the three Δ*ftsZ* strains had 20- to 25-fold fewer colony-forming units (c.f.u.) compared with the wild type (Fig. 2a), consistent with a larger cell size and/or a decreased fraction of viable cells. The Δ*ftsZ* strains displayed very heterogeneously sized and misshapen cells, as well as a substantial quantity of cellular debris (Fig. 2b,c), very similar to the respective *p.tna–ftsZ* strains grown continuously without Trp (Supplementary Fig. 3a). The Δ*ftsZ2* and Δ*ftsZ1* Δ*ftsZ2* strains showed more severe cell division defects compared with Δ*ftsZ1*, indicating that FtsZ2 has a limited capacity to support division in the absence of FtsZ1 (Fig. 2b,c). The equally low c.f.u. count of Δ*ftsZ1* therefore suggests that FtsZ1 may have additional functions that contribute to cell survival or growth. Furthermore, the relatively moderate FtsZ1 depletion cell division phenotype (Fig. 1a) appears to be largely caused by differing roles of FtsZ1 and FtsZ2 rather than the differences in depletion rate (Fig. 1b).

The genome sequence data for H98 and the three knockout strains showed several small sequence variations of no known or expected consequences (Supplementary Table 5). We therefore sought to verify the attribution of the above phenotypes specifically to *ftsZ1* and/or *ftsZ2* by reintroducing these genes, under the control of the *p.tna* promoter on a plasmid (based on pTA962), into the corresponding deletion mutants. In all three cases, this successfully complemented the cell division and growth rate defects in the presence of 0.2 mM Trp induction or greater (Fig. 2g, Extended Data Fig. 4 and Supplementary Fig. 5). At relatively high concentrations of Trp (1 or 2 mM), the strains expressing *ftsZ1* showed some rods or spindle-like cell shapes (investigated further below).

The apparent correlation between the appearance of greatly enlarged cells and debris (<1 μm³; Fig. 2c) suggested that the largest cells produce cell fragments or disintegrate to form the debris. Interestingly, Δ*ftsZ1* Δ*ftsZ2* also showed a greater frequency of highly elongated filamentous cells (31%) compared with the plate-like cell shapes seen in mid-log cultures of the wild type and two single

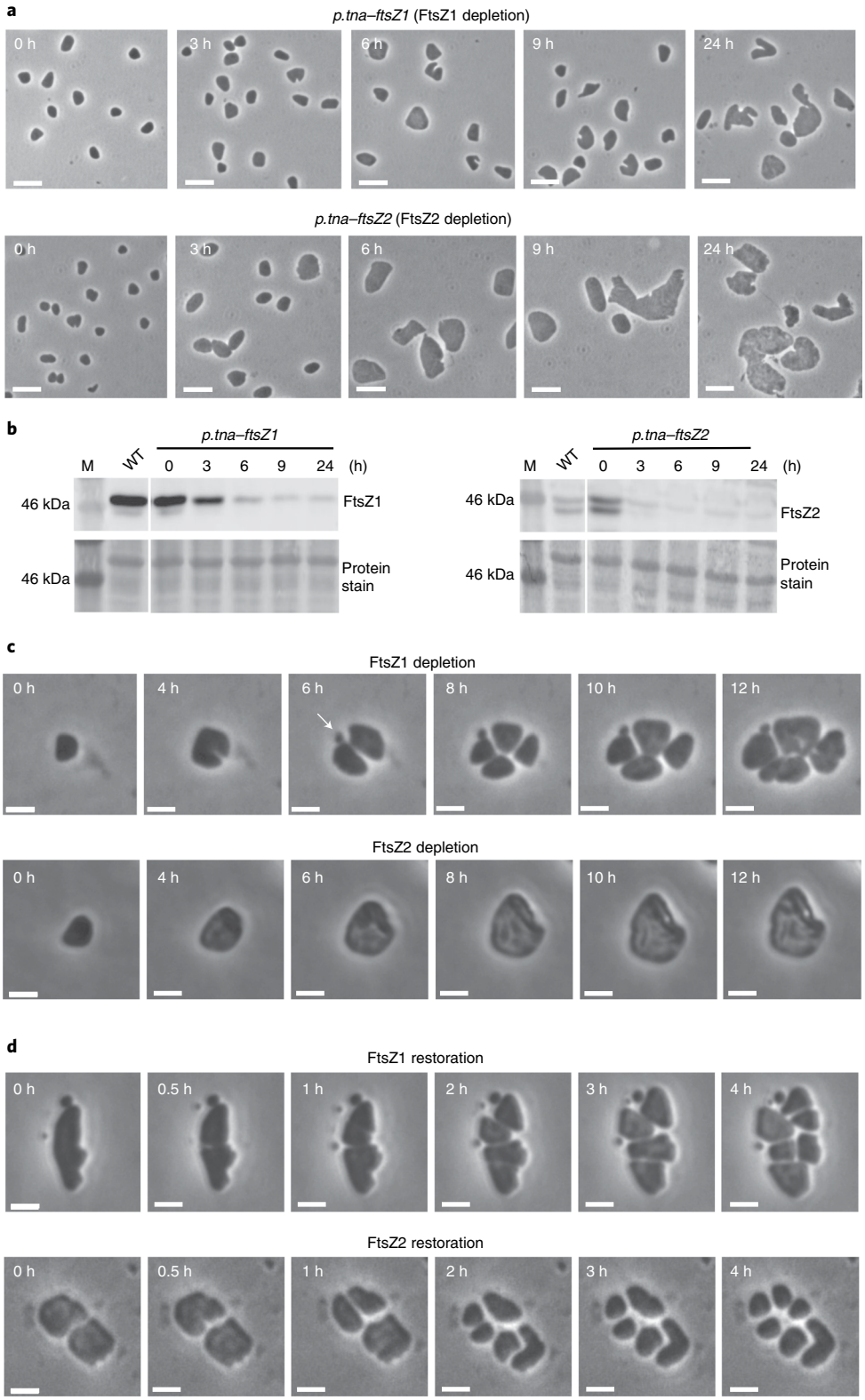

Fig. 1 | Depletion of FtsZ1 or FtsZ2 results in cell division defects. a, Phase-contrast microscopy images of samples from cultures (*H. volcanii* ID56 (*p.tna–ftsZ1*) and ID57 (*p.tna–ftsZ2*)) immediately before (0 h) or at the indicated time points after resuspension of cells (to $OD_{600} = 0.25$) in growth medium without Trp. Scale bars, 5 µm. **b**, Western blots probed with FtsZ1 (left) or FtsZ2 (right) antisera during depletion with the corresponding Ponceau S pre-staining of total protein. The separate H26 wild-type (WT) lanes were from the same blots for each protein; bands for the ~46-kDa pre-stained marker (M) and FtsZ1 (expected ~40 kDa) and FtsZ2 (expected ~43 kDa) are indicated. The double band, which is clearer for FtsZ2, suggests modified or clipped forms. **c**, In situ time-lapse imaging of FtsZ depletion. Cells cultured in Hv-Cab + 2 mM Trp were washed and placed onto agarose media pads without Trp and imaged over time. The morphology of giant cells differs from the liquid culture in **a**, probably due to the support provided by growth on agarose. Scale bars, 2 µm **d**, In situ time-lapse imaging of FtsZ restoration. The respective *p.tna–ftsZ* strains were initially grown for ~2 d without Trp inducer, then the cells were washed and placed onto agarose media (Hv-Cab) pads including 0.2 mM Trp for FtsZ1 and 2 mM Trp for FtsZ2. Scale bars, 2 µm.

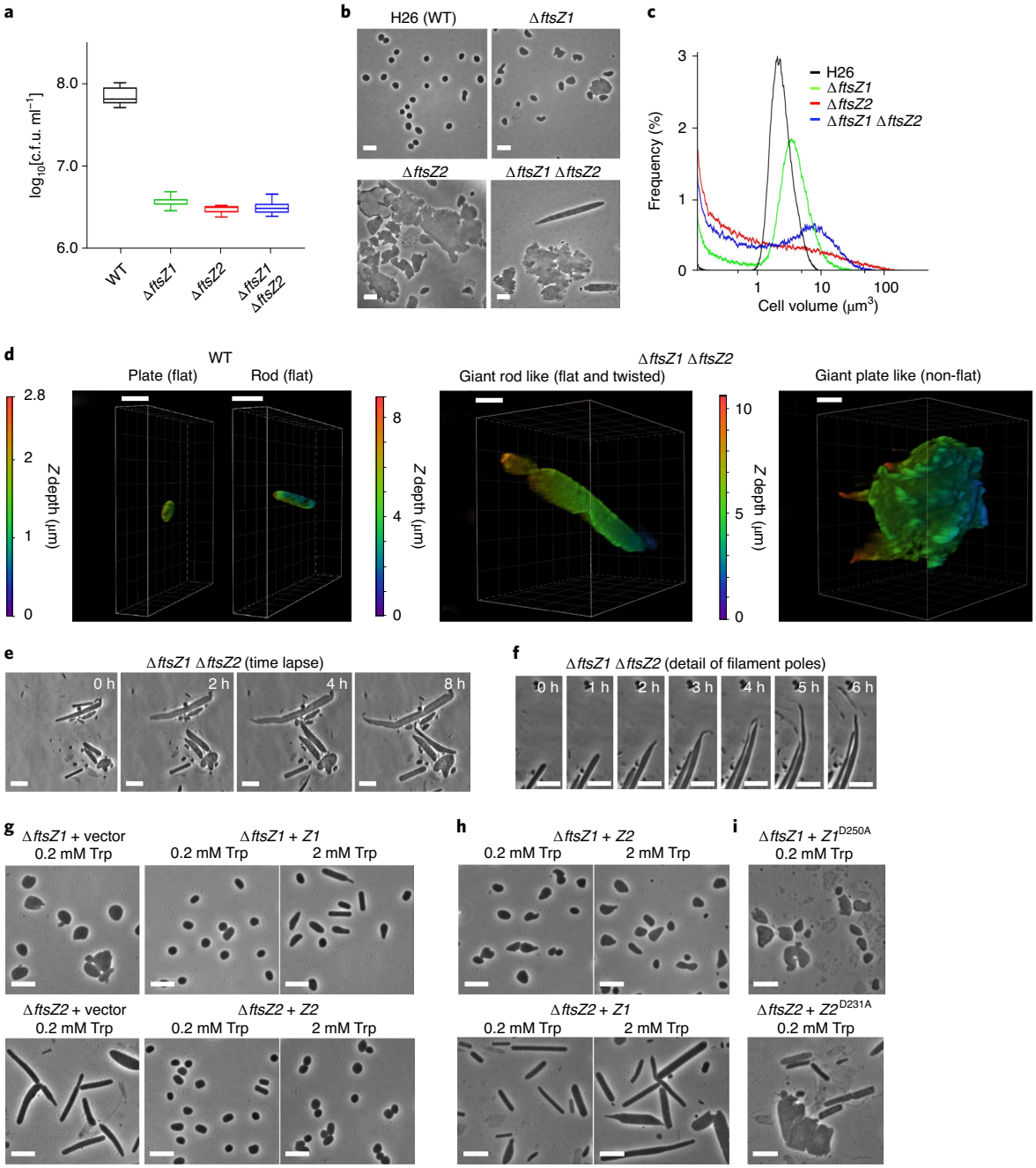

Fig. 2 | FtsZ1 and FtsZ2 are dispensable for survival but required for normal cell division. a, Box plots of agar colony counts of the *H. volcanii* wild type (H26), Δ*ftsZ1* (ID76), Δ*ftsZ2* (ID77) and Δ*ftsZ1*Δ*ftsZ2* (ID112), sampled during mid-log growth (OD_{600} = 0.2) in Hv-Cab medium (+50 μg ml^{-1} uracil) (n = 4 separate cultures; n = 3 for Δ*ftsZ1*Δ*ftsZ2*; one experiment). The box edges show the interquartile range, the whiskers represent the upper and lower limits and the central lines are the median values. **b**,**c**, Phase-contrast images (**b**) and Coulter cell volume frequency distributions (normalized to total count) (**c**). Scale bars in **b**, 5 μm. **d**, Confocal microscopy 3D-reconstructed images of cells stained with MitoTracker Orange and embedded in low-melting-point agarose. The reconstructions are shown with a rotation of ~45° around the *x* axis. Scale bars, 2 μm. Similar morphologies were seen with FM1-43 membrane staining (Supplementary Fig. 4b). **e**,**f**, Live-cell time-lapse images of Δ*ftsZ1*Δ*ftsZ2* growing on an agarose media pad (**e**) and showing polar tubulation and budding-like processes (**f**). Scale bars, 5 μm. **g**–**i**, Phase-contrast microscopy of the indicated strains expressing the *ftsZ* genes or containing vector only in steady mid-log cultures with Hv-Cab medium and the indicated concentrations of Trp. Scale bars, 5 μm.

Δ*ftsZ* strains (<1% filaments) (Fig. 2b and Supplementary Fig. 4c). *H. volcanii* shapes can be readily influenced by several conditions or stresses[24] (see Supplementary Results and Discussion) and the two major categories of giant cells appear to be the result of division defects in the common plate and rods morphotypes, respectively. The filamentous Δ*ftsZ1* Δ*ftsZ2* cells showed a similar flattened shape profile to the wild-type rod- and plate-shaped cells, which are normally ~0.5 μm thick (Fig. 2d and Supplementary Video 4). However, the giant plate-like cells had lost much of the flatness of the wild type and displayed multi-lobed ramified three-dimensional (3D) morphologies (Fig. 2d, Supplementary Fig. 4b and Supplementary Video 4), underscoring the remarkable plasticity of the *H. volcanii*

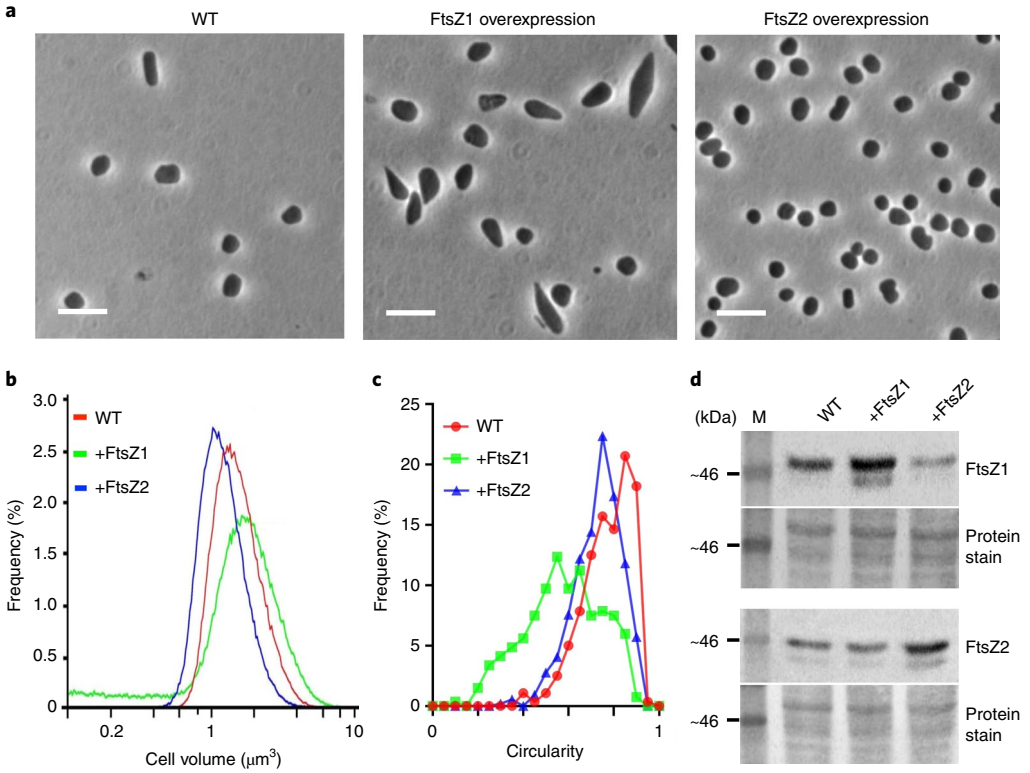

Fig. 3 | Overproduction of FtsZ1 or FtsZ2 differentially affects cell division and shape. a. Phase-contrast micrographs of the *H. volcanii* wild type (H98 + pTA962), ID25 (FtsZ1 overproduction; H98 + pTA962-*ftsZ1*) and ID26 (FtsZ2 overproduction; H98 + pTA962-*ftsZ2*) from steady mid-log cultures in Hv-Cab + 2 mM Trp. Scale bars, 5 μm. **b**, Coulter cell volume frequency distributions (normalized to total count) of the strains in **a**. **c**, Frequency distributions of the circularity of cell outlines, generated from analysis of the microscopy data from a representative experiment with the following numbers of cells: $n = 280$ (wild type); $n = 267$ (+FtsZ1); $n = 541$ (+FtsZ2). **d**, Western blots and Ponceau total protein staining of whole-cell lysates of the wild-type, FtsZ1 overproduction and FtsZ2 overproduction strains, probed with FtsZ1 or FtsZ2 antisera, as indicated. The ~46-kDa size marker (M) is indicated.

envelope in the giant cells. This could lead to abiotic division or cell disintegration/fragmentation in a turbulent environment, and could account for some of the highly irregular morphologies observed when cells are transferred from liquid to an agarose gel surface (for example, Figs. 1a and 2b).

To further assess the capacity of cells to survive without *ftsZ*, including potential propagation via alternative biotic processes, mid-log samples were transferred to soft agarose media pads for imaging of the cells during growth (Fig. 2e, Supplementary Fig. 4d and Supplementary Videos 5–8). Under these conditions, the mutants grew substantially larger (over ~12 h), indicating that the cells were structurally stabilized by the gel compared with the previous liquid culture (Fig. 2c). Nevertheless, while some Δ*ftsZ1* cells grew very large (Supplementary Video 5), others divided, often very acentrally or with a crooked division plane (Supplementary Video 6). Division was not seen in Δ*ftsZ2* cells, which expanded to extremely large sizes, and rare blebbing was seen (Supplementary Video 7). Interestingly, the filaments common in Δ*ftsZ1* Δ*ftsZ2* showed substantial polar narrowing and extension (tubulation), followed by fission to produce much smaller fragments (Fig. 2e,f and Supplementary Video 8). These samples also contained many small particles, which may be the product of the polar tubulation and fission or fragmentation in previous culture. The fragmentation, budding, tubulation and fission and, in the case of Δ*ftsZ1*, occasional inaccurate division appear to result in particles, at least some of which contain DNA (Extended Data Fig. 3a), that produce enough viable cells for culture propagation in the absence of normal cell division.

Overexpression of *ftsZ1* or *ftsZ2* causes contrasting phenotypes and cannot properly compensate for loss of the other. If FtsZ1 and FtsZ2 have different roles in division, overexpression of each could exacerbate aspects of each protein's specific activities and potentially lead to different effects. Furthermore, if overexpression of *ftsZ2* in the Δ*ftsZ1* strain, and vice versa, corrects the division defects (that is, cross-complementation), this would indicate similar or overlapping functions of the two proteins. FtsZ1 overproduction in the wild-type background caused enlarged cells, indicating inefficient or misregulated division (Fig. 3). It also caused a change in cell shape, where cells frequently displayed a rod-like appearance or a noticeable taper at one or both poles (Fig. 3c). In contrast, FtsZ2 overproduction resulted in smaller cells than the wild type, indicating that FtsZ2 overproduction stimulates division, with no specific influence on cell shape (Fig. 3).

FtsZ1 overproduction provided no detectable recovery to the Δ*ftsZ2* division defect (Fig. 2h and Supplementary Fig. 6), but caused increased debris and some striking spindle-like cell shapes with rather pointy poles or various angular morphologies, as well as very long filamentous cells of approximately normal rod cell width. The spindly cells therefore appear to be associated with FtsZ1 overproduction in the wild-type, Δ*ftsZ1* and Δ*ftsZ2* backgrounds (Figs. 2g,h and 3a and Supplementary Fig. 7). FtsZ2 overproduction caused weak complementation of the Δ*ftsZ1* division defect (Fig. 2g,h and Supplementary Figs. 5 and 6), indicating partial compensation for the missing FtsZ1 or a capacity to take on some of the role(s) of FtsZ1 in division. These findings show

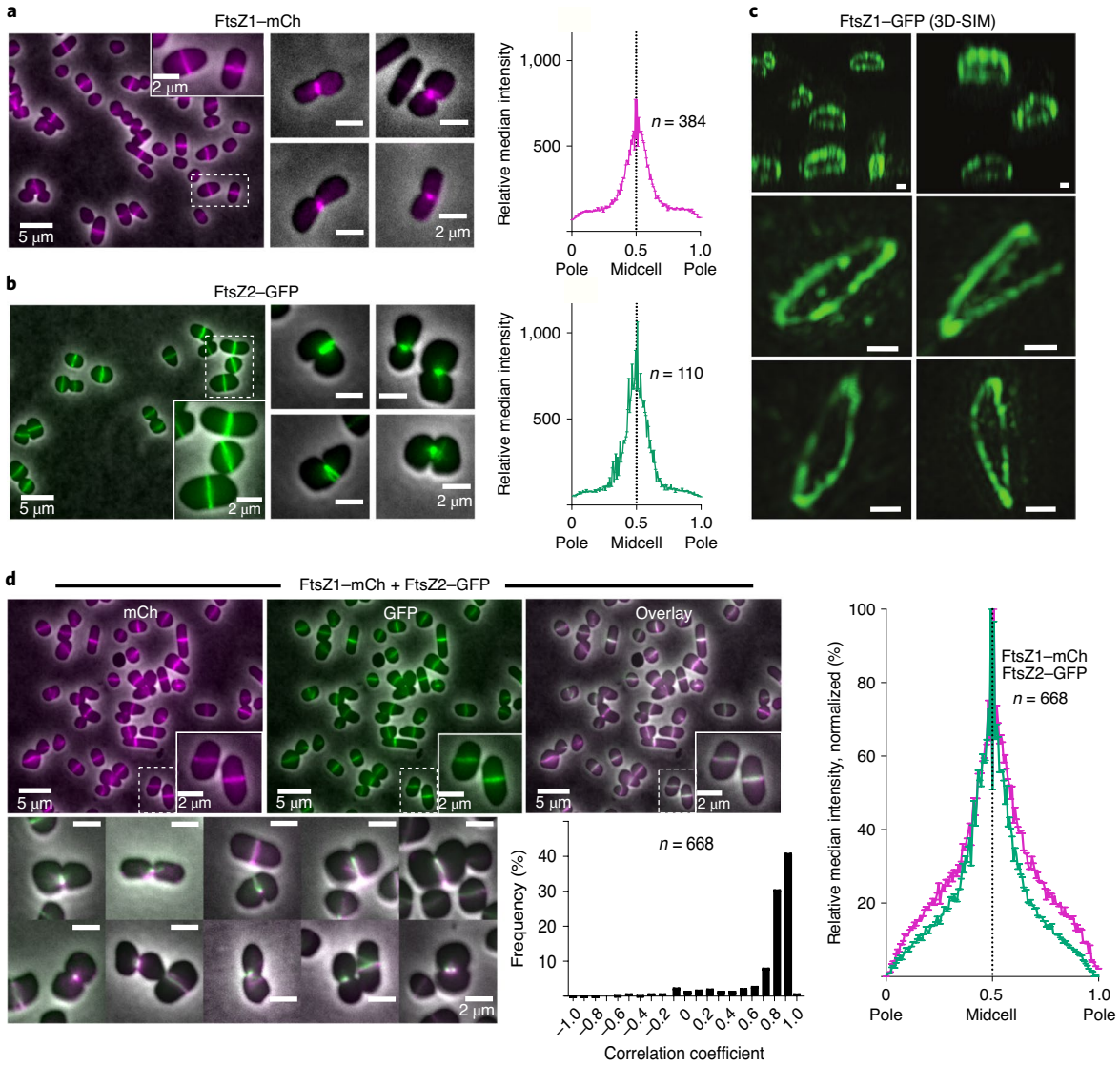

Fig. 4 | Midcell localization of FtsZ1 and FtsZ2. a,**b**,**d**, Mid-log cultures of *H. volcanii* ID49 (WT + FtsZ1-mCh) (**a**), ID17 (WT + FtsZ2-GFP) (**b**) and ID67 (WT + FtsZ1-mCh + FtsZ2-GFP dual localization) (**d**), cultured with 0.2 mM Trp, were imaged by phase-contrast and fluorescence microscopy. mCh (magenta) and GFP (green) fluorescence was quantified along the long axis of cells by plotting the relative (normalized) median intensity perpendicular to the long axis. Panel **d** also shows selected examples of dividing cells (bottom left). The ring containing FtsZ1 and FtsZ2 closes down with division constrictions, which range from unilateral to partially and equally bilateral. The middle graph shows correlation coefficients plotted as a frequency distribution (80% of the cells had a correlation coefficient of ≥0.7). The total number of cells analysed (*n*) were obtained with data from two independent experiments. The intensity data (right) are presented as median values, with error bars showing the upper and lower limits. **c**, 3D-SIM micrographs of mid-log *H. volcanii* ID16 (WT + FtsZ1-GFP) (Hv-Cab + 0.2 mM Trp). The top two panels show a side-on view (~70° tilt of the *x*–*y* view) whereas the lower four panels show an *x*–*y* tilt of ~20°. Scale bars, 300 nm.

that FtsZ1 and FtsZ2 have differing functions, and that FtsZ2 has a key active role in the constriction mechanism, whereas FtsZ1 has a supporting role. Consistent with this, as *ftsZ1* mutant cultures slowed growth and entered the stationary phase, the cell size recovered to nearly normal, but this did not occur in *ftsZ2* mutants (Extended Data Fig. 5).

Predicted GTPase active site (T7 loop) residues are essential for FtsZ1 and FtsZ2 functions. FtsZ1 and FtsZ2 both contain the conserved GTP-binding domain and catalytic residues in the T7 loop (see Extended Data Fig. 1d) that are needed for GTP hydrolysis and correct function of FtsZ/tubulin polymers[31,32]. Bacterial FtsZ studies have shown that point mutations of the T7 catalytic residues block GTPase-dependent filament disassembly, thus forming hyper-stable filaments that can coassemble with the wild-type protein and severely disrupt function[33–35]. Overproduction of an equivalent aspartate-to-alanine variant of FtsZ1 (p.Asp250Ala substitution in the T7 loop) inhibited division in *H. volcanii*[20]. To determine whether both FtsZ1 and FtsZ2 require their predicted GTPase catalytic residues for their functions in division, we expressed *ftsZ1*^{D250A} and the equivalent *ftsZ2*^{D231A} mutant from plasmids in their corresponding Δ*ftsZ* backgrounds. These mutants completely failed to complement the division defects (Fig. 2i). The Δ*ftsZ1* + *ftsZ1*^{D250A} combination clearly exacerbated the Δ*ftsZ1* defect (Fig. 2b,c and Supplementary Fig. 8a). Similarly, Δ*ftsZ2* + *ftsZ2*^{D231A} displayed a mix of giant plates and cell debris, but also showed filaments at the early- to mid-stages of culture (Fig. 2i and Supplementary Fig. 8b). The additional phenotypes associated with

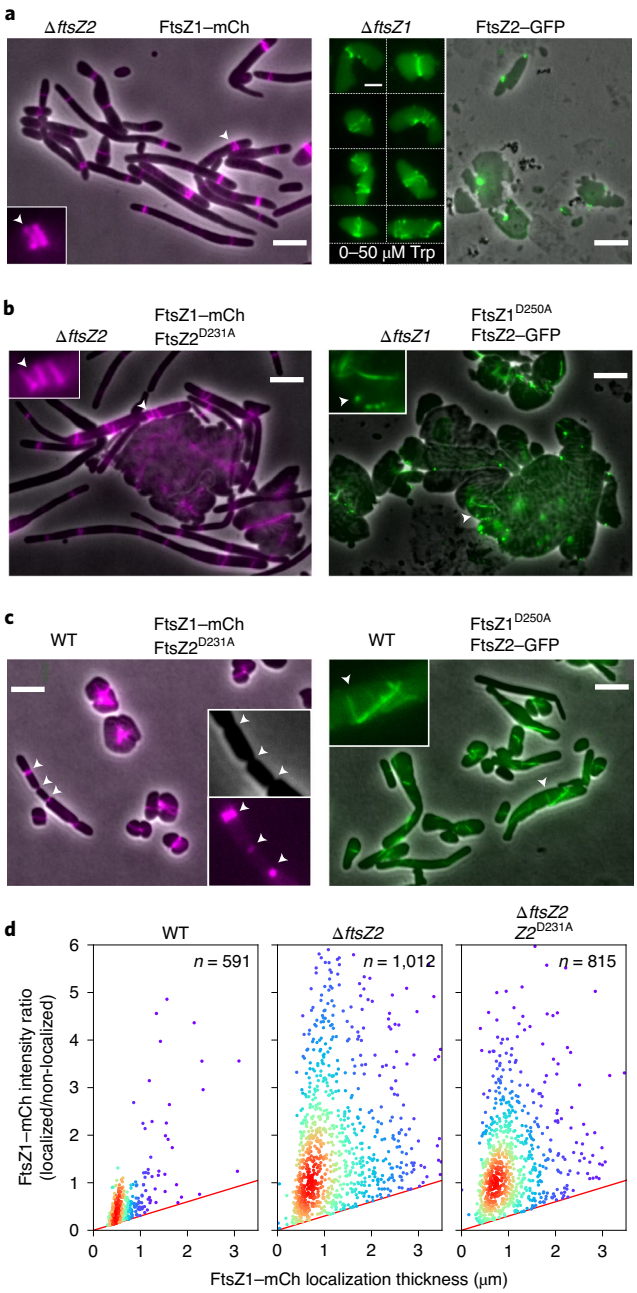

Fig. 5 | Localization interdependency and the effect of *ftsZ* mutations on FtsZ1-mCh and FtsZ2-GFP localization. Fluorescence and phase-contrast microscopy was used to examine mid-log *H. volcanii* strains (wild-type or Δ*ftsZ* backgrounds) carrying plasmid copies of the indicated *ftsZ* mutants and fusion proteins. Strains were grown with 0.2 mM Trp unless otherwise specified. Insets either show a magnified view of the area identified by an arrowhead in the main panel or represent another culture grown with the indicated concentration of Trp (right panel in **a**). **a**, Localization of each FtsZ in the absence of the other FtsZ. Inset scale bar (right image), 2 μm. **b**, Localization of each FtsZ in the presence of the T7 mutant as the sole copy of the other FtsZ. **c**, Localization of each FtsZ in the wild-type genomic background expressing the T7 mutant of the other FtsZ. Scale bars in **a**–**c** (main images), 5 μm. **d**, Ratio of individual FtsZ1-mCh localization intensity over the mean cellular background fluorescence versus localization thickness (μm) in rods or filaments in the indicated backgrounds. The data points are coloured with a proximity heatmap. Representative images of the wild-type background are provided in Fig. 4a.

expression of the two point mutants suggested that they actively interfere with division or the cell envelope. Indeed, even moderate expression of *ftsZ1*^{D250A} or *ftsZ2*^{D231A} caused strong division defects in the wild-type background (Supplementary Fig. 9). We therefore sought to investigate the subcellular localization and assembly of the wild-type and mutant proteins.

Subcellular localization of FtsZ1 and FtsZ2. Genes encoding the fluorescent proteins GFP and mCherry (mCh) were fused to the C termini of FtsZ1 and FtsZ2. FtsZ1–GFP or FtsZ1–mCh produced from plasmids (with 0.2 mM Trp) partially complemented the cell division defect of the Δ*ftsZ1* strain (Extended Data Fig. 6a); many cells showed normal size and shape, with a fluorescent band at the midcell or division constriction, whereas others were larger and occasionally misshapen with more complex fluorescent structures near the midcell. FtsZ2–GFP failed to complement the Δ*ftsZ2* division defect, but the highly filamentous cells showed sporadic FtsZ2–GFP foci or rings that were seen ~3–4 μm from a pole (Extended Data Fig. 6b), suggestive of the influence of a division site positioning mechanism[28] that is sensitive to pole proximity.

Functional interference from fluorescent proteins is very common in FtsZ and tubulin[36–38]. Since the FtsZ fusion proteins were not fully functional in division as the sole copy, but did localize, we reasoned that they could be useful localization markers and not substantially perturb cell division in the presence of the wild-type FtsZ (as seen in bacteria). Indeed, low-level induction of FtsZ1 or FtsZ2 tagged with mCh or GFP in a wild-type background did not disturb normal cell size and shape. FtsZ1–mCh localized as a band at the midcell or division constriction in almost all cells (Fig. 4a), with no evidence of perturbed division at 0.2 and 1 mM Trp (Extended Data Fig. 6c). Similarly, FtsZ2–GFP localized at the midcell or division constriction in almost all cells, which appeared normal or slightly enlarged with 0.2 mM Trp (Fig. 4b and Extended Data Fig. 6d). With 1 mM Trp, cells producing FtsZ2–GFP were substantially enlarged, and some had aberrant FtsZ2–GFP clusters near the centre, consistent with their detachment from the envelope (Fig. 4b and Extended Data Fig. 6d).

We confirmed the expected flattened ring-like structure of the midcell bands by imaging FtsZ1–GFP in the wild-type background with 3D structured-illumination microscopy (3D-SIM; Fig. 4c (top two images); ~70° *x*–*y* tilt). This also revealed patchy, discontinuous rings or short helical structures (Fig. 4c (bottom four images); ~20° *x*–*y* tilt), similar to the appearance of bacterial Z rings[39,40]. Time-lapse imaging showed that the uneven fluorescence intensity of FtsZ1–GFP around the ring was dynamic during the cell cycle (Supplementary Videos 9 and 10) and confirmed that prompt reassembly of new rings occurs after division in orientations consistent with predictions from cell morphology[28].

When produced together, FtsZ1–mCh and FtsZ2–GFP generally colocalized as a midcell band in essentially all cells (Fig. 4d and Extended Data Fig. 6e), indicating that both proteins assemble into a midcell band very soon after the previous division and are maintained at the midcell during cell growth. Colocalization was strong, with a correlation coefficient of >0.8 in the majority of cells, but appeared noticeably imperfect in some (Fig. 4d). The two proteins contracted together during division, which varied from bilateral to unilateral (Fig. 4), and remained generally colocalized during reassembly over several cell cycles (Fig. 4d and Supplementary Video 11).

Differing interdependency of FtsZ1 and FtsZ2 localization. The differing functions of FtsZ1 and FtsZ2 in division, and their colocalization at the midcell, prompted us to investigate the dependency of FtsZ1 and FtsZ2 on each other for cellular localization and assembly, by visualizing each FtsZ–FP in the alternate Δ*ftsZ* and T7-loop mutant backgrounds. The T7 mutations were expected to produce

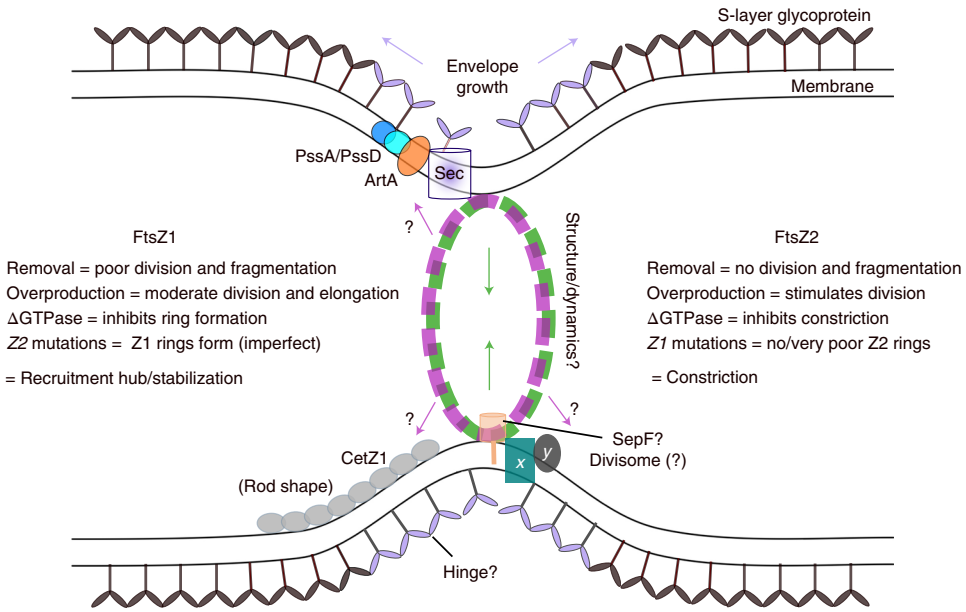

Fig. 6 | Model of FtsZ1 and FtsZ2 function at the archaeal division site. Schematic of FtsZ1 (magenta) and FtsZ2 (green) localization and functions (arrows), based on our results. Most archaea, including *H. volcanii*, have an envelope composed of a lipid membrane and an S-layer glycoprotein semi-crystalline array on the surface. Our results raise questions about the ultrastructure and dynamics of the two FtsZ proteins in the division ring, the identity of an unknown number of other putative divisome components (*x*, *y* and a SepF homologue) and how the ring could functionally associate with the envelope growth (Sec/PssA/PssD/ArtA) and cell shape regulation (CetZ1) machineries, which appear to be spatially and functionally linked to the midcell[20,41].

aberrant hyper-stable polymers and could help to resolve individual functions in divisome assembly or constriction.

In the absence of *ftsZ2*, FtsZ1–mCh displayed one or more clear rings (Fig. 5a) in the predominantly filamentous cells (62%; Extended Data Fig. 7a). The localizations were spaced every ~5 µm on average and some appeared less condensed than normal rings—as a short helicoid or irregular structure (Fig. 5a and Extended Data Fig. 8). Giant plate-like cells were also present (5%), which contained clusters of FtsZ1–mCh (similar to that seen in Fig. 5b). In the absence of *ftsZ1*, FtsZ2–GFP formed patches, foci or short filaments, but no rings (0.2 mM Trp; Fig. 5a). This strain showed a much more severe division defect than Δ*ftsZ1* and Δ*ftsZ1* + unlabelled FtsZ2 (Fig. 2g–h). To minimize this strong inhibitory effect of the FtsZ2–GFP, we used lower induction levels (0 or 50 µM Trp) and indeed observed some cells with poorly formed midcell structures, which appeared as more normal rings in dividing cells (Fig. 5a and Supplementary Fig. 10). Since FtsZ2–GFP induced with 0.2 mM Trp had only a very minor effect on division when FtsZ1 was present (Fig. 4b and Extended Data Fig. 6d,e), and at higher levels (1 mM Trp) it inhibited division and appeared to inhibit envelope association (Extended Data Fig. 6d), FtsZ1 must counteract the destabilizing effect of FtsZ2–GFP on normal FtsZ2 assembly. Taken together, these results strongly suggest that FtsZ1 can assemble independent of FtsZ2 and promotes and stabilizes proper FtsZ2 assembly for division at the midcell envelope.

When FtsZ2^{D231A} was produced as the sole copy of FtsZ2 (in Δ*ftsZ2*) with FtsZ1–mCh, highly elongated cells were observed (Fig. 5b and Extended Data Fig. 7b), similar to the unlabelled strain (Fig. 2i), and FtsZ1–mCh localizations again appeared as rings, broader zones or helicoid structures (Fig. 5b). Measurements of the FtsZ1–mCh localization intensity (compared with the cellular background) and individual localization thickness in the filaments (Fig. 5d) confirmed the lack of condensation of some of the FtsZ1 localizations in the FtsZ2 variants and revealed that a substantially higher proportion of the FtsZ1–mCh was localized in the absence of wild-type FtsZ2, compared with the wild-type background. These findings suggest that FtsZ2 contributes to proper divisome condensation or maturation and may limit the incorporation of FtsZ1 into the ring. In the less frequent giant plates (Fig. 5b), FtsZ1–mCh showed separate filaments or diffuse clusters, or rarely appeared as an apparent ring spanning the cell, probably due to a lack of spatial cues for positioning the division machinery in the giant malformed cells[28] and a low probability of assembling a ring of such abnormal size. When FtsZ1^{D250A} was produced as the sole copy of FtsZ1 (Fig. 5b), the cells formed giant plates, as expected, and FtsZ2–GFP displayed patches or foci and some filaments, but no rings. Overall, the moderate influence of the sole T7 mutants on the other FtsZ's localization pattern, compared with the respective knockout background (Fig. 5a), suggests that the sole-copy T7 mutant proteins do not efficiently homopolymerize, or they do not efficiently interact (or interfere) with the other FtsZ.

Highly informative results were obtained with the wild-type background. In this setting, production of FtsZ2^{D231A} with FtsZ1–mCh partly inhibited division during constriction—the enlarged cells often displayed one or more incomplete constrictions with FtsZ1–mCh rings or occasional irregular structures present at those sites (Fig. 5c; left). This strongly suggests that FtsZ2^{D231A} mixes with wild-type FtsZ2 to inhibit GTPase-dependent constriction, and that the primary function of FtsZ2 and its GTPase activity is therefore division constriction. In contrast, production of FtsZ1^{D250A} with FtsZ2–GFP in the wild-type background caused obvious aberrant filaments containing FtsZ2–GFP, which were orientated seemingly at random or with the longer cell axis (Fig. 5c; right). Clearly, the presence of wild-type FtsZ1 in this strain allows the assembly of aberrant filaments caused by FtsZ1^{D250A}, which recruit FtsZ2–GFP (compare Fig. 5a–c; right), leading us to conclude that FtsZ2's subcellular localization is strongly influenced by FtsZ1. Furthermore, the absence of both midcell localization and partial constrictions (Fig. 5c; right) indicates that the primary function of FtsZ1 and its GTPase activity is the proper assembly of the division machinery.

Next, we aimed to simultaneously visualize both the T7 mutant of one FtsZ and the wild-type copy of the other. However, to our surprise, FP tagging of the T7 mutants suppressed their dominant inhibitory phenotypes, but they still localized in midcell rings (Extended Data Fig. 9c,d) and partly colocalized with the alternative wild-type FtsZ–FP (Extended Data Fig. 10 and Supplementary Information). It would appear that FP-tagged T7 mutants only assemble into a type of filament that can associate with but not inhibit the divisome. The combined data further supported the view that: (1) FtsZ1 localization is largely independent of FtsZ2; (2) FtsZ2 assembly, positioning and stabilization are heavily dependent on the presence, localization and correct functioning of FtsZ1; and (3) FtsZ1 ring condensation (via a helicoid intermediate) is in turn promoted by feedback from the presence and correct functioning of FtsZ2.

Discussion

We have shown that archaeal FtsZ1 and FtsZ2, from distinct families within the tubulin superfamily of cytoskeletal/cytomotive proteins, both localize to the division ring but have different mechanistic roles. FtsZ1 assembles largely independent of FtsZ2 and directs the assembly, stabilization and correct localization of FtsZ2, whereas FtsZ2 is critical during constriction, including divisome activation or structure (see Fig. 6).

FtsZ1 was also capable of stimulating the formation of rod and tapered morphologies from the common plate/disc morphotype. *H. volcanii* rods also form during CetZ1 overproduction[20], and CetZ1 can also localize at the midcell or as filaments along the cell edge perpendicular to the division plane during its key function in rod development. Our findings suggest a possible linkage between FtsZ1 and CetZ1 function in promoting cell elongation (Fig. 6). Furthermore, nascent S-layer glycoprotein and the PssA/PssD/ArtA enzymes required for its lipid modification and proper membrane anchoring were recently found to localize at the midcell, and blocking this pathway caused rod formation but did not affect division[41]. These findings suggest a model in which FtsZ1 creates a scaffold or platform at the midcell that acts as a hub or landmark to recruit and stabilize the division, shape and envelope biosynthesis machineries.

Despite these important functions in division and shape, *H. volcanii* lacking both FtsZs could be cultured indefinitely with standard solid and liquid media. FtsZ is thought to be essential for division and survival in almost all walled bacteria[25], but under specific conditions of wall removal (L forms) or excess envelope—causing cell ramification—they can produce viable fragments and propagate without FtsZ[42,43]. *H. volcanii* Δ*ftsZ* strains appear similar (Fig. 2). Most archaea have a lipid membrane and a flexible glycoprotein S layer but no cell wall as in peptidoglycan-enclosed bacteria[44]. Considering the morphological plasticity of wild-type *H. volcanii*[24] and the Δ*ftsZ* strains, a turbulent liquid environment may be expected to promote physical fragmentation or disintegration of the giant cells, from which any particles with a complete genome may be viable and contribute to propagation without proper cytokinesis. We imagine that such abiotic division could have helped sustain very early life on Earth. Our results also suggest that budding and polar tubulation fission might contribute to survival, and similar non-FtsZ modes of proliferation can occur in wall-less bacteria[45–48]. *H. volcanii*, and potentially other wall-less archaea, should therefore be suitable for studying primitive or alternative division modes and the normal cellular functions underlying them.

While the two FtsZs are conserved in the majority of surveyed archaea (Supplementary Table 3), six of the 41 complete genomes encode only one FtsZ each. Remarkably, we noticed that the same six species, from the classes Methanobacteria and Methanopyri, are the only ones known to have a pseudomurein wall analogous to bacterial peptidoglycan (murein) (Supplementary Table 3)[49,50]. Furthermore, these classes only encode FtsZ1 homologues. The archaeal dual FtsZ system therefore appears to have evolved after an early paralogous gene duplication, then FtsZ2 was lost when pseudomurein evolved in those lineages.

In bacteria, division appears to be primarily driven by FtsZ-directed ingrowth of the peptidoglycan cell wall[3,4], and possibly an additional constriction force on the cytoplasmic membrane[5,6]. Electron microscopy of Methanobacteria and Methanopyri shows a clear septal wall during division that is very similar in appearance to that seen in bacteria[51–53]. Archaea without pseudomurein show a division furrow instead[54,55], and with only a single flexible S layer (a 2D semi-crystalline protein array), the archaeal envelope is almost certainly not capable of providing the same directionality or structural persistence that remodelling of the covalent peptidoglycan mesh would in bacterial septal ingrowth[56]. Our experimental results and the clear phylogenetic association strongly suggest that FtsZ2 is required for constriction where there is no covalent wall ingrowth to impose directionality to division. We therefore predict that a division complex containing FtsZ2 at its core provides an intrinsic constriction force on the flexible archaeal envelope. With the low or no turgor pressure in wall-less archaea, especially halophilic archaea[57], this force might be sufficient to complete division[7].

Given the functional differentiation of two FtsZs in archaeal cell division, and the corresponding lack of a cell wall, we propose that *H. volcanii* provides a powerful model for mechanistic studies of cell division to contrast against the well-studied bacterial models with peptidoglycan. We anticipate that this will contribute to establishing the underlying and primordial principles of FtsZ-based division across the domains of life and help unravel some of the mysteries of early cellular evolution and division.

Methods

Identification, phylogeny and analysis of FtsZ sequences and structure. Thirteen known FtsZ protein sequences from bacteria and plants were aligned with MUSCLE[58] for use as the search set to identify homologues in a diverse collection of 60 archaeal genomes (Supplementary Table 3) by searching their respective Reference Proteome or UniProt databases using JackHMMER[59]. All significant hits were selected, excluding several redundancies and low-quality sequences, and they were then aligned, together with the search set, using MUSCLE. The identification of homologues belonging to either the archaeal FtsZ1, FtsZ2, CetZ or other categories was done based on the position of individual sequences in a maximum likelihood phylogenetic tree, obtained using MEGA (version 7.0.26)[60] with 100 bootstrap replicates, based on the alignment containing only those sites with >25% occupancy. *H. volcanii* FtsZ1 (HVO_0717), FtsZ2 (HVO_0581) and CetZ1 (HVO_2204) were taken as the reference sequences for identifying the three families.

To determine the percentage sequence identities for each of the four domains, as defined for *H. volcanii* FtsZ1 and FtsZ2 in Extended Data Fig. 1b, the sequence alignment generated above was arranged into protein families, including only those proteins classifying as FtsZ1, FtsZ2 or CetZ, and was then separated into individual domain alignments using Jalview (version 2.9.0b2)[61]. Each set was individually realigned with MUSCLE and used as input for generating a ClustalX percentage identity matrix[62] that was used for determining means. The crystal structure of *M. jannaschii* FtsZ1 (ref. [63]; Protein Data Bank code: 1FSZ) was displayed with PyMol (version 1.7).

Growth of *H. volcanii*. Most experimental *H. volcanii* cultures were grown in Hv-Cab medium[20], or Hv-YPC medium for some genetic modification procedures[64]. Where necessary as auxotrophic requirements, media were supplemented with uracil (10 or 50 μg ml^{-1}) for Δ*pyrE2* strains or thymidine and hypoxanthine (40 μg ml^{-1} each) for Δ*hdrB* strains. Cultures were incubated at 45 °C with rotary shaking (200 r.p.m.) and were generally maintained in continuous logarithmic growth (OD_{600} < 0.8) for at least 2 d before sampling for analysis of mid-log cultures, unless otherwise indicated. To control gene expression via the *p.tna* promoter, the indicated concentration of L-Trp (Sigma–Aldrich) was included in these cultures.

Genomic modification. The strains used in this study and the plasmids used to construct them are listed in Supplementary Tables 1 and 2, respectively. To generate strains allowing Trp-controlled expression of *ftsZ1* or *ftsZ2* for the depletion studies (Supplementary Fig. 1), two respective plasmids were first constructed that can recombine with each corresponding genomic *ftsZ* locus using two-step homologous recombination[64], thereby substituting the normal transcriptional regulation of *ftsZ* with the specific Trp-inducible *p.tna* promoter. First, the

upstream and downstream flanks for homologous recombination on either side of each *ftsZ* gene's start codon were PCR amplified from *H. volcanii* DS2 genomic DNA (upstream flank) and the corresponding pIDJL40–*ftsZ* plasmid (downstream flank, containing the L11e transcription terminator and *p.tna–ftsZ* cassette to be inserted), using the primers given in Supplementary Table 2. The upstream and downstream fragments in each case were joined by overlap-extension PCR and the products were digested with HindIII and BamHI (sites located in the end primers; Supplementary Fig. 1 and Supplementary Table 2) and ligated to pTA131 (at HindIII–BamHI), giving pIDJL74 (*p.tna–ftsZ1*) and pIDJL75 (*p.tna–ftsZ2*). For *ftsZ1*, the sequence of the chosen upstream flank would result in a 39-base pair (bp) deletion of genomic DNA immediately upstream of the *ftsZ1* start codon during the replacement. For *ftsZ2*, which is located as the second gene in a predicted operon (downstream of HVO_0582, with a 2-bp gap), no genomic DNA was deleted when inserting the *p.tna* construct upstream of the *ftsZ2* open reading frame (ORF). To allow direct selection of the *p.tna–ftsZ* genomic replacements, the BamHI fragment from pTA1185 (T. Allers, personal communication), containing *p.fdx–hdrB*[64], was inserted at the BglII site in pIDJL74 and pIDJL75 (that is, between the upstream and downstream fragments, described above). Clones containing *p.fdx–hdrB* co-directional with the downstream *p.tna–ftsZ* cassette were selected and named pIDJL96 (*ftsZ1*) and pIDJL97 (*ftsZ2*) (Supplementary Table 2).

Demethylated pIDJL96 and pIDJL97 (obtained via passage through *E. coli* C2925) were used to transform *H. volcanii* H98 separately, selecting isolated colonies that grew on agar medium (without uracil), which were expected to contain the plasmid integrated by single-crossover (pop-in)[64] between the upstream or downstream flank and the corresponding genomic *ftsZ* locus. After growth of single colonies in liquid media (minus uracil), cells were plated onto Hv-Ca agar containing 10 μg ml^{-1} uracil, 50 μg ml^{-1} 5-fluoroorotic acid and 0.5 mM Trp, to select for recombinational excision of these non-replicative plasmids (pop-out)[64], which, following gene conversion, left the cassette containing *p.fdx–hdrB* and *p.tna–ftsZ* as the only copy of *ftsZ*; single colonies were streaked onto the same medium, then arising colonies were screened by allele-specific PCR to verify the expected chromosomal structure, giving strains ID56 (*p.tna–ftsZ1*) and ID57 (*p.tna–ftsZ2*) (Supplementary Table 1).

To construct plasmids for the deletion of each *ftsZ* gene, PCR fragments of downstream flanking DNA for *ftsZ1* and *ftsZ2* were amplified (the primers are shown in Supplementary Table 2). The products were digested with BglII and BamHI, then ligated, respectively, to the large fragments of pIDJL74 or pIDJL75 digested with BglII, BamHI and alkaline phosphatase. Isolated clones containing the appropriate co-orientation of up- and downstream flanks were selected and named pIDJL128 (*ftsZ1* flanks) and pIDJL129 (*ftsZ2* flanks) (Supplementary Table 2). These plasmids were then digested with BglII (that is, cutting between the flanks), then the *p.fdx–hdrB* BamHI fragment from pTA1185 was ligated to them, generating pIDJL142 (for *ftsZ1* deletion) and pIDJL143 (for *ftsZ2* deletion).

To delete *ftsZ* and/or *ftsZ2* in *H. volcanii*, plasmids pIDJL142 and pIDJL143, respectively, were demethylated as described above, then used to transform *H. volcanii* H98 using the two-step procedure noted above[64], yielding strains ID76 (that is, (H98) Δ*ftsZ1–p.fdx–hdrB*) and ID77 (that is, (H98) Δ*ftsZ2–p.fdx–hdrB*). Then, to construct the double knockout strain, *H. volcanii* ID77 was transformed with demethylated pIDJL128 (Supplementary Table 2) using the two-step method described above, generating *H. volcanii* ID112. The expected mutations were verified by allele-specific PCR and genome sequencing, as described below, to detect the presence of the expected *ftsZ* deletion allele and the absence of the wild-type allele(s). In addition, the expected lack of the corresponding proteins was verified with western blotting using specific FtsZ1 or FtsZ2 antibodies (Extended Data Fig. 4 and Supplementary Fig. 5d).

Genome sequencing and variant calling. Whole-genome sequencing libraries for strains H98, ID76, ID77 and ID112 were prepared using the Illumina Nextera Flex DNA kit with custom index primers. Sequencing fragment libraries were then pooled and size selected using SPRISelect magnetic beads (Beckman Coulter) and the pooled library was then quality checked and quantified with an Agilent Bioanalyzer 2100 using the High Sensitivity DNA kit (Agilent). Sequencing was performed using an Illumina MiSeq system with a 300-cycle micro flow cell with V2 chemistry. Sequence data were demultiplexed using PhyloSift[65] and trimmed using Trimmomatic with default settings[66]. A draft H98 genome was assembled using the A5-miseq assembler (version 20150522)[67], then the trimmed reads for the three Δ*ftsZ* strains were aligned to the draft H98 genome using bwa[68]. Variant calling was done using bcftools mpileup and call[69]. Any single-nucleotide polymorphisms that had a quality score of <20 or were located within contigs of <1,000 bp were discarded. Non-synonymous variants in coding regions or any variants in intergenic regions were then identified in ID76, ID77 and ID112 compared with the H98 draft reference genome (Supplementary Table 5).

Construction of plasmids for gene expression in *H. volcanii*. All of the plasmids and the primers used in their construction are listed in Supplementary Table 2. The plasmids pTA962 (ref. [70]) or pIDJL40 (containing GFP)[20] were used as the basis to construct plasmids for controlled expression of the *ftsZ* genes or modified versions. To construct pTA962–*ftsZ1*, the *ftsZ1* ORF (HVO_0717) was amplified from *H. volcanii* DS70 genomic DNA using primers *ftsZ1-f* and *ftsZ-r*, then the product was cloned between the NdeI and BamHI sites of pTA962. pTA962–*ftsZ2* was constructed in the same way, except with primers *ftsZ2-f* and *ftsZ2-r* to amplify the *ftsZ2* ORF (HVO_0581). The *ftsZ1*^{D250A} mutation was constructed previously[20] and the *ftsZ2*^{D231A} mutation was similarly made by overlap-extension PCR using the mutational primers and primers *ftsZ2-f* and *ftsZ2-r* and the product cloned between NdeI and BamHI in pTA962.

The wild-type and mutant *ftsZ* ORFs were also amplified without their stop codons, then cloned between the NdeI and BamHI sites of pIDJL40, to create *ftsZ–gfp* fusions (linker encoding GS, derived from the BamHI site). Then, to construct *ftsZ1–mCh* and *ftsZ2–mCh* fusions (pIDJL114 and pIDJL115, respectively), the GFP fragments in pIDJL40–*ftsZ1* and pIDJL40–*ftsZ2* were replaced with a BamHI–NotI fragment encoding a linker (GSAGSAAGSGEF, including the initial BamHI site and ending EcoRI site) and mCh, as described previously[20]. To construct plasmids for expression of the mutant *ftsZ* genes tagged with mCh, NdeI + BamHI fragments (containing the point mutant *ftsZ* genes without their stop codons) were ligated to the large fragment of pIDJL117 (that is, expression of *cetZ1–mCh*) digested with NdeI and BamHI, thus replacing the *cetZ1* with the mutant *ftsZ*. The expected DNA sequences of all cloned PCR products and point mutations in this study were verified by Sanger sequencing.

For dual expression of the various *ftsZ* genes, PvuII fragments from the above plasmids (containing a *p.tna–ftsZ* gene fusion) were ligated into HindIII-cut (Klenow blunt-ended) plasmids containing the other *ftsZ* gene for the required combination, creating plasmids with two independent copies of the different *p.tna–ftsZ* fusions; the combinations made are given in Supplementary Table 2, where the second-listed gene in the description refers to the one transferred secondarily in the PvuII fragment. All plasmids were demethylated by passage through *E. coli* C2925 and re-purified before transfer to *H. volcanii* by polyethylene glycol-mediated spheroplast transformation[64].

Growth curves (microtitre plate) and colony (c.f.u.) counting. Cultures maintained in log growth for at least 2 d were diluted to an OD_{600} of 0.005 with fresh medium, then 150 μl volumes were dispensed into a BD Falcon 96-well culture plate per well. The absorbance (OD_{600}) of the samples over time was measured with a Tecan Spark 10 M microplate spectrophotometer at 42 °C with orbital shaking (amplitude = 2.5 mm; 216 r.p.m.), with readings every 30 min for 56 h. Representative data from one of four independent experiments were then plotted, displaying standard error bars for technical replicates of the OD_{600} at each time point. Colonies (c.f.u.) were determined by taking mid-log samples of each strain at OD_{600} = 0.2, then plating 100-μl volumes of serial dilutions onto Hv-Cab (+50 μg ml^{-1} uracil) agar. Colonies were then counted after 4–5 d incubation in a sealed bag at 45 °C.

Microscopy. For transmitted light and epifluorescence microscopy, a 1- or 2-μl sample of culture was placed on a 1% agarose pad containing 18% buffered saltwater (BSW) on a glass slide at room temperature, and a #1.5 glass coverslip was placed on top. Images were acquired using a 1.4-numerical aperture oil immersion objective with phase-contrast or differential-interference-contrast transmission optics, or by epifluorescence with GFP (Excitation filter = 475/28 nm; Emission filter = 525/48 nm) or mCh (Excitation filter = 632/22 nm; Emission filter = 676/34 nm) filter sets. 3D-SIM was performed as previously described[20].

For live-cell time-lapse imaging, the submerged sandwich technique (for the growth of cells on agarose pads[20]) or a microfluidics platform was used. For agarose pads, 1–2 μl of mid-log culture was placed on a gel pad with a thickness of ~1 mm (0.3% wt/vol agarose containing the complete medium for the required conditions), which had been prepared on an 8-mm-diameter #1.5 circular glass coverslip (WPI). The coverslip–pad–sample assembly was then lifted with forceps and placed, inverted, onto the base of a 35-mm glass-based (#1.5) FluoroDish (WPI). Pre-warmed liquid medium (3 ml) was then gently applied to cover the pad assembly on the base, and the lid was applied to avoid evaporation. For microfluidics, a CellASIC ONIX system was used with bacterial microfluidic plates (B04A; EMD Millipore). The flow cells were first equilibrated with 1 mg ml^{-1} bovine serum albumin in phosphate-buffered saline followed by 18% BSW at a constant flow pressure of 5 p.s.i. Cells were loaded into the chamber and perfused with the indicated medium and pressure. Time-lapse imaging was performed at 42 or 45 °C on a Nikon Ti-E microscope with a 1.45-numerical aperture oil immersion phase-contrast objective, maintaining focus automatically during time lapse.

For 3D confocal imaging, live cells were stained by addition of the cytoplasmic vital stain MitoTracker Orange (1 μM)[71] to mid-log cultures at ~18 h (45 °C with shaking) before washing the cells three times and resuspending in fresh medium (without stain), or by addition of the membrane dye FM1-43 (5 μg ml^{-1}) to culture samples at 45 °C for 15 min. The stained cells were then gently mixed with an equal volume of molten (45 °C) 1% low-melting-point agarose in fresh growth medium and the mixture was placed onto the base of a FluoroDish. The environment was maintained humidified with a wet tissue during imaging at 37 or 45 °C. A Nikon A1 laser-scanning confocal microscope was used with a 488-nm laser Z step of 0.2 μm. Each 3D confocal series was deconvolved by NIS-Elements software (AR 4.60.00; Nikon) using blind deconvolution (20 iterations). The 3D volume visualization was rendered using depth-coded alpha blending to display the depth information, followed by the blind deconvolution process for 20 iterations. The 3D

video animations were created by rotation around the *y* axis with a display rate of 20 frames per second.

Image analysis. To determine cell circularity, phase-contrast images were first smoothed using a Gaussian filter followed by a rolling-ball background subtraction in FIJI[72]. Individual objects (cells) were then identified by thresholding and filling any holes. Clearly touching cells were manually separated. The minimum cell area was 0.2 μm^2 and objects overlapping the image edge were excluded. The cell area was obtained from the analyze particles function, and cell circularity was calculated by determining each cell's bounding disc coverage (the percentage area of the cell within the minimal circle that completely contained the cell outline[20]) with a custom script in FIJI. Cells and particles were classified as filaments (cell area > 7.5 μm^2; circularity < 0.3), giant plates (cell area > 7.5 μm^2; circularity > 0.3), wild-type-like cells (any shape, with a cell area between 1.5 and 7.5 μm^2) or cellular debris (<1.5 μm^2), as indicated in the graphs.

FtsZ1 and FtsZ2 medial localization along the cell long axis (Fig. 4) was determined with FIJI[72] and MicrobeJ[73]. Fluorescent images were pre-treated with the background subtraction filter (ballsize 8) in FIJI. Cell outlines were detected in MicrobeJ by phase-contrast image segmentation using the Otsu method, with the medial axis mode, area > 0.98 and exclude-on-edges options, then manually corrected where needed. Fluorescence foci were detected using the Foci and Smoothed modes with a tolerance of 160, a *z* score of 8 and an area of >0.005. Raw pixel intensities and medial profiles were recorded. Data were output using the MicrobeJ XStatProfile Plot function with the following parameters: Stat: Median, *y* axis: MEDIAL.intensity.ch1 (and 2 for colocalization), bin#:150. The correlation coefficients for individual cells for FtsZ1–mCh and FtsZ2–GFP fluorescence were obtained using the following MicrobeJ statistics functions: Stat.: count, Data: EXPERIMENT.count.total. Split horizontal: INTENSITY.ch2.correlation.ch1.

To determine FtsZ1–mCh localization frequency, intensity and thickness (Fig. 5 and Extended Data Fig. 8), cell outlines (regions of interest) were first obtained from the phase-contrast channel in FIJI, by combining automated detection and manual curation. The long medial axis for rods and filaments was then identified, and the fluorescence channel data (after image/sensor background subtraction) were then quantified by averaging the intensity along the transverse axis to create a longitudinal intensity profile for each cell. Gaussian peaks were fitted to the detected localizations and a spline was fit to the cellular fluorescence background. The localization thickness was taken as the width of the fitted Gaussian peaks at half height (μm), the localization intensity was taken as the area under the curve (minus the background) and the background intensity was taken as the area under each corresponding peak (averaged over the whole cell).

Coulter and flow cytometry. For Coulter cytometry to obtain cell volume distributions, culture samples were diluted (1:100 or 1:1,000) with 0.2-μm-filtered 18% BSW and analysed with a Multisizer M4 Coulter cytometer (Beckman Coulter) equipped with a 20- or 30-μm aperture tube, running and calibrated with 2-μm latex beads in 18% BSW as the electrolyte. Runs were completed in the volumetric mode (100 μl), with a current of 600 μA and a gain of 4. For flow cytometry, mid-log culture samples were diluted 1:10 with a solution of 5 μM SYTOX Green in 18% BSW and incubated at room temperature for ~30 min before log-scale data acquisition (triggered by a side-scatter threshold) with an LSR II flow cytometer (BD) with 18% BSW as the sheath fluid. The cell sampling size normally ranged between 30,000 and 100,000 events per sample.

Western blotting. Rabbit antisera for the detection of *H. volcanii* FtsZ1 and FtsZ2 were generated with a synthetic peptide antigen derived from the sequence of the C-terminal region of FtsZ1 (QAHAEERLEDIDYVE; Cambridge Research Biochemicals), used at 1:1,000 dilution of serum. For FtsZ2, antibodies were raised against a peptide containing an N-terminally derived sequence (ERQTQSSLEDSDDQFGDPR; Thermo Fisher; 1:500 dilution of serum) and one derived from the C-terminal region (SDGGRDEVEKNNGLDVIR; Thermo Fisher; 1:4,000 dilution of affinity-purified antibody stock of 2.95 mg ml^{-1}). The FtsZ2 antibodies were used either as diluted serum or affinity-purified protein (selecting for binding for the target peptide) as follows: N terminus (serum): Fig. 1b and Supplementary Figs. 3c, 5d and 6c; C terminus (affinity purified): Fig. 3d and Extended Data Fig. 4b. *H. volcanii* cell pellets (separated from any excess liquid medium) were resuspended in SDS–PAGE sample buffer, then the samples were heated (95 °C; 5 min) and vortexed. Samples were separated by SDS–PAGE, then electroblotted (Bio-Rad) on a nitrocellulose membrane (Protran; Whatman) and probed with the rabbit polyclonal primary antibodies described above, followed by secondary antibody (donkey anti-rabbit IgG-HRP; AbCam 16284; 1:5,000 dilution), with standard techniques. Bands were detected with enhanced chemiluminescence reagents (Thermo Fisher) using an Amersham Imager 600 system.

Reporting Summary. Further information on research design is available in the Nature Research Reporting Summary linked to this article.

Data availability

The NCBI (www.ncbi.nlm.nih.gov/protein/) and UniProt (www.uniprot.org) protein sequence databases were searched to obtain sequences of archaeal tubulin superfamily proteins. Genome sequence data generated in this study have been deposited in the NCBI BioProject database under the identifier PRJNA681931. Source data are provided with this paper. Other data and biological materials are available from the corresponding author upon reasonable request.

Received: 16 June 2020; Accepted: 22 March 2021;
Published online: 26 April 2021

References

1. Adams, D. W. & Errington, J. Bacterial cell division: assembly, maintenance and disassembly of the Z ring. *Nat. Rev. Microbiol.* **7**, 642–653 (2009).
2. Du, S. & Lutkenhaus, J. Assembly and activation of the *Escherichia coli* divisome. *Mol. Microbiol.* **105**, 177–187 (2017).
3. Bisson-Filho, A. W. et al. Treadmilling by FtsZ filaments drives peptidoglycan synthesis and bacterial cell division. *Science* **355**, 739–743 (2017).
4. Yang, X. et al. GTPase activity-coupled treadmilling of the bacterial tubulin FtsZ organizes septal cell wall synthesis. *Science* **355**, 744–747 (2017).
5. Osawa, M., Anderson, D. E. & Erickson, H. P. Reconstitution of contractile FtsZ rings in liposomes. *Science* **320**, 792–794 (2008).
6. Szwedziak, P., Wang, Q., Bharat, T. A., Tsim, M. & Lowe, J. Architecture of the ring formed by the tubulin homologue FtsZ in bacterial cell division. *eLife* **3**, e04601 (2014).
7. Osawa, M. & Erickson, H. P. Turgor pressure and possible constriction mechanisms in bacterial division. *Front. Microbiol.* **9**, 111 (2018).
8. Zhou, X. et al. Bacterial division. Mechanical crack propagation drives millisecond daughter cell separation in *Staphylococcus aureus*. *Science* **348**, 574–578 (2015).
9. Typas, A., Banzhaf, M., Gross, C. A. & Vollmer, W. From the regulation of peptidoglycan synthesis to bacterial growth and morphology. *Nat. Rev. Microbiol.* **10**, 123–136 (2012).
10. Margolin, W., Wang, R. & Kumar, M. Isolation of an *ftsZ* homolog from the archaebacterium *Halobacterium salinarium*: implications for the evolution of FtsZ and tubulin. *J. Bacteriol.* **178**, 1320–1327 (1996).
11. Wang, X. & Lutkenhaus, J. FtsZ ring: the eubacterial division apparatus conserved in archaebacteria. *Mol. Microbiol.* **21**, 313–319 (1996).
12. Baumann, P. & Jackson, S. P. An archaebacterial homologue of the essential eubacterial cell division protein FtsZ. *Proc. Natl Acad. Sci. USA* **93**, 6726–6730 (1996).
13. Poplawski, A., Gullbrand, B. & Bernander, R. The *ftsZ* gene of *Haloferax mediterranei*: sequence, conserved gene order, and visualization of the FtsZ ring. *Gene* **242**, 357–367 (2000).
14. Krupka, M. & Margolin, W. Unite to divide: oligomerization of tubulin and actin homologs regulates initiation of bacterial cell division. *F1000Res.* **7**, 235 (2018).
15. Duman, R. et al. Structural and genetic analyses reveal the protein SepF as a new membrane anchor for the Z ring. *Proc. Natl Acad. Sci. USA* **110**, E4601–E4610 (2013).
16. Makarova, K. S. & Koonin, E. V. Two new families of the FtsZ-tubulin protein superfamily implicated in membrane remodeling in diverse bacteria and archaea. *Biol. Direct* **5**, 33 (2010).
17. Bult, C. J. et al. Complete genome sequence of the methanogenic archaeon, *Methanococcus jannaschii*. *Science* **273**, 1058–1073 (1996).
18. Lindas, A. C., Karlsson, E. A., Lindgren, M. T., Ettema, T. J. & Bernander, R. A unique cell division machinery in the Archaea. *Proc. Natl Acad. Sci. USA* **105**, 18942–18946 (2008).
19. Samson, R. Y., Obita, T., Freund, S. M., Williams, R. L. & Bell, S. D. A role for the ESCRT system in cell division in Archaea. *Science* **322**, 1710–1713 (2008).
20. Duggin, I. G. et al. CetZ tubulin-like proteins control archaeal cell shape. *Nature* **519**, 362–365 (2015).
21. Aylett, C. H. S. & Duggin, I. G. The tubulin superfamily in archaea. *Subcell. Biochem.* **84**, 393–417 (2017).
22. Hartman, A. L. et al. The complete genome sequence of *Haloferax volcanii* DS2, a model archaeon. *PLoS ONE* **5**, e9605 (2010).
23. Bisson-Filho, A. W., Zheng, J. & Garner, E. Archaeal imaging: leading the hunt for new discoveries. *Mol. Biol. Cell* **29**, 1675–1681 (2018).
24. de Silva, R. T. et al. Improved growth and morphological plasticity of *Haloferax volcanii*. *Microbiology* https://doi.org/10.1099/mic.0.001012 (2021).
25. Erickson, H. P. & Osawa, M. Cell division without FtsZ—a variety of redundant mechanisms. *Mol. Microbiol.* **78**, 267–270 (2010).
26. Large, A. et al. Characterization of a tightly controlled promoter of the halophilic archaeon *Haloferax volcanii* and its use in the analysis of the essential *cct1* gene. *Mol. Microbiol.* **66**, 1092–1106 (2007).
27. Slater, M. & Schaechter, M. Control of cell division in bacteria. *Bacteriol. Rev.* **38**, 199–221 (1974).
28. Walsh, J. C. et al. Division plane placement in pleomorphic archaea is dynamically coupled to cell shape. *Mol. Microbiol.* **112**, 785–799 (2019).
29. Breuert, S., Allers, T., Spohn, G. & Soppa, J. Regulated polyploidy in halophilic archaea. *PLoS ONE* **1**, e92 (2006).

30. Delmas, S., Duggin, I. G. & Allers, T. DNA damage induces nucleoid compaction via the Mre11–Rad50 complex in the archaeon *Haloferax volcanii*. *Mol. Microbiol.* **87**, 168–179 (2013).
31. Coltharp, C. & Xiao, J. Beyond force generation: why is a dynamic ring of FtsZ polymers essential for bacterial cytokinesis? *Bioessays* **39**, 1–11 (2017).
32. Nogales, E., Downing, K. H., Amos, L. A. & Lowe, J. Tubulin and FtsZ form a distinct family of GTPases. *Nat. Struct. Biol.* **5**, 451–458 (1998).
33. Chen, Y., Bjornson, K., Redick, S. D. & Erickson, H. P. A rapid fluorescence assay for FtsZ assembly indicates cooperative assembly with a dimer nucleus. *Biophys. J.* **88**, 505–514 (2005).
34. Scheffers, D. J., de Wit, J. G., den Blaauwen, T. & Driessen, A. J. GTP hydrolysis of cell division protein FtsZ: evidence that the active site is formed by the association of monomers. *Biochemistry* **41**, 521–529 (2002).
35. Scheffers, D. J., de Wit, J. G., den Blaauwen, T. & Driessen, A. J. Substitution of a conserved aspartate allows cation-induced polymerization of FtsZ. *FEBS Lett.* **494**, 34–37 (2001).
36. Kimble, M., Kuzmiak, C., McGovern, K. N. & de Hostos, E. L. Microtubule organization and the effects of GFP–tubulin expression in *Dictyostelium discoideum*. *Cell Motil. Cytoskeleton* **47**, 48–62 (2000).
37. Moore, D. A., Whatley, Z. N., Joshi, C. P., Osawa, M. & Erickson, H. P. Probing for binding regions of the FtsZ protein surface through site-directed insertions: discovery of fully functional FtsZ-fluorescent proteins. *J. Bacteriol.* **199**, e00553-16 (2016).
38. Sun, Q. & Margolin, W. FtsZ dynamics during the division cycle of live *Escherichia coli* cells. *J. Bacteriol.* **180**, 2050–2056 (1998).
39. Rowlett, V. W. & Margolin, W. 3D-SIM super-resolution of FtsZ and its membrane tethers in *Escherichia coli* cells. *Biophys. J.* **107**, L17–L20 (2014).
40. Strauss, M. P. et al. 3D-SIM super resolution microscopy reveals a bead-like arrangement for FtsZ and the division machinery: implications for triggering cytokinesis. *PLoS Biol.* **10**, e1001389 (2012).
41. Abdul-Halim, M. F. et al. Lipid anchoring of archaeosortase substrates and midcell growth in haloarchaea. *mBio* **11**, e00349-20 (2020).
42. Leaver, M., Dominguez-Cuevas, P., Coxhead, J. M., Daniel, R. A. & Errington, J. Life without a wall or division machine in *Bacillus subtilis*. *Nature* **457**, 849–853 (2009).
43. Mercier, R., Kawai, Y. & Errington, J. Wall proficient *E. coli* capable of sustained growth in the absence of the Z-ring division machine. *Nat. Microbiol.* **1**, 16091 (2016).
44. Albers, S. V. & Meyer, B. H. The archaeal cell envelope. *Nat. Rev. Microbiol.* **9**, 414–426 (2011).
45. Abdelrahman, Y., Ouellette, S. P., Belland, R. J. & Cox, J. V. Polarized cell division of *Chlamydia trachomatis*. *PLoS Pathog.* **12**, e1005822 (2016).
46. Errington, J. L-form bacteria, cell walls and the origins of life. *Open Biol.* **3**, 120143 (2013).
47. Lluch-Senar, M., Querol, E. & Pinol, J. Cell division in a minimal bacterium in the absence of ftsZ. *Mol. Microbiol.* **78**, 278–289 (2010).
48. Rivas-Marin, E. et al. Non-essentiality of canonical cell division genes in the planctomycete *Planctopirus limnophila*. *Sci. Rep.* **10**, 66 (2020).
49. Steenbakkers, P. J., Geerts, W. J., Ayman-Oz, N. A. & Keltjens, J. T. Identification of pseudomurein cell wall binding domains. *Mol. Microbiol.* **62**, 1618–1630 (2006).
50. Visweswaran, G. R., Dijkstra, B. W. & Kok, J. Murein and pseudomurein cell wall binding domains of bacteria and archaea—a comparative view. *Appl. Microbiol. Biotechnol.* **92**, 921–928 (2011).
51. Burggraf, S., Stetter, K. O., Rouviere, P. & Woese, C. R. *Methanopyrus kandleri*: an archaeal methanogen unrelated to all other known methanogens. *Syst. Appl. Microbiol.* **14**, 346–351 (1991).
52. Zeikus, J. G. The biology of methanogenic bacteria. *Bacteriol. Rev.* **41**, 514–541 (1977).
53. Zeikus, J. G. & Wolfe, R. S. Fine structure of *Methanobacterium thermoautotrophicum*: effect of growth temperature on morphology and ultrastructure. *J. Bacteriol.* **113**, 461–467 (1973).
54. Dobro, M. J. et al. Electron cryotomography of ESCRT assemblies and dividing *Sulfolobus* cells suggests that spiraling filaments are involved in membrane scission. *Mol. Biol. Cell* **24**, 2319–2327 (2013).
55. Mullakhanbhai, M. F. & Larsen, H. *Halobacterium volcanii* spec. *nov*., a Dead Sea halobacterium with a moderate salt requirement. *Arch. Microbiol.* **104**, 207–214 (1975).
56. Liao, Y., Ithurbide, S., de Silva, R. T., Erdmann, S. & Duggin, I. G. Archaeal cell biology: diverse functions of tubulin-like cytoskeletal proteins at the cell envelope. *Emerg. Top. Life Sci.* **2**, 547–559 (2018).
57. Walsby, A. E. & Fogg, G. E. The pressure relationships of gas vacuoles. *Proc. R. Soc. Lond. B Biol. Sci.* **178**, 301–326 (1971).
58. Edgar, R. C. MUSCLE: multiple sequence alignment with high accuracy and high throughput. *Nucleic Acids Res.* **32**, 1792–1797 (2004).
59. Potter, S. C. et al. HMMER web server: 2018 update. *Nucleic Acids Res.* **46**, W200–W204 (2018).
60. Kumar, S., Stecher, G., Li, M., Knyaz, C. & Tamura, K. MEGA X: molecular evolutionary genetics analysis across computing platforms. *Mol. Biol. Evol.* **35**, 1547–1549 (2018).
61. Waterhouse, A. M., Procter, J. B., Martin, D. M., Clamp, M. & Barton, G. J. Jalview Version 2—a multiple sequence alignment editor and analysis workbench. *Bioinformatics* **25**, 1189–1191 (2009).
62. Thompson, J. D., Gibson, T. J. & Higgins, D. G. Multiple sequence alignment using ClustalW and ClustalX. *Curr. Protoc. Bioinformatics* **Ch. 2**, Unit 2.3 (2002).
63. Löwe, J. Crystal structure determination of FtsZ from *Methanococcus jannaschii*. *J. Struct. Biol.* **124**, 235–243 (1998).
64. Allers, T., Ngo, H. P., Mevarech, M. & Lloyd, R. G. Development of additional selectable markers for the halophilic archaeon *Haloferax volcanii* based on the *leuB* and *trpA* genes. *Appl. Environ. Microbiol.* **70**, 943–953 (2004).
65. Darling, A. E. et al. PhyloSift: phylogenetic analysis of genomes and metagenomes. *PeerJ* **2**, e243 (2014).
66. Bolger, A. M., Lohse, M. & Usadel, B. Trimmomatic: a flexible trimmer for Illumina sequence data. *Bioinformatics* **30**, 2114–2120 (2014).
67. Coil, D., Jospin, G. & Darling, A. E. A5-miseq: an updated pipeline to assemble microbial genomes from Illumina MiSeq data. *Bioinformatics* **31**, 587–589 (2015).
68. Li, H. & Durbin, R. Fast and accurate short read alignment with Burrows–Wheeler transform. *Bioinformatics* **25**, 1754–1760 (2009).
69. Li, H. et al. The sequence alignment/map format and SAMtools. *Bioinformatics* **25**, 2078–2079 (2009).
70. Allers, T., Barak, S., Liddell, S., Wardell, K. & Mevarech, M. Improved strains and plasmid vectors for conditional overexpression of His-tagged proteins in *Haloferax volcanii*. *Appl. Environ. Microbiol.* **76**, 1759–1769 (2010).
71. Maslov, I. et al. Efficient non-cytotoxic fluorescent staining of halophiles. *Sci. Rep.* **8**, 2549 (2018).
72. Schindelin, J. et al. Fiji: an open-source platform for biological-image analysis. *Nat. Methods* **9**, 676–682 (2012).
73. Ducret, A., Quardokus, E. M. & Brun, Y. V. MicrobeJ, a tool for high throughput bacterial cell detection and quantitative analysis. *Nat. Microbiol.* **1**, 16077 (2016).

Acknowledgements

This study was supported by the Australian Research Council (FT160100010 to I.G.D.) and UK Biotechnology and Biological Sciences Research Council (BBSRC) and Medical Research Council (U105184326 to J.L.). For technical support, we thank L. Turnbull, M. Johnson and L. Cole (from the UTS Microbial Imaging Facility) and K. Anantanawat and M. Liu (from the UTS DNA Sequencing Facility).

Author contributions

I.G.D., S.I., Y.L. and J.L. designed the research. I.G.D., S.I. and Y.L. collected the preliminary data and constructed the strains. The following authors contributed and analysed the data: Y.L. (Figs. 1, 2b–i, 3, 5a and 6, Extended Data Figs. 2, 4 and 5, Supplementary Figs. 1–8 and 10, Supplementary Table 5 and Supplementary Videos 1–10), S.I. (Figs. 2a, 4a,b,d, 5a–d and 6, Extended Data Figs. 6–10, Supplementary Figs. 4 and 9–11, Supplementary Tables 1 and 2 and Supplementary Video 11), I.G.D. (Figs. 4c, 5a,d and 6, Extended Data Figs. 1, 3 and 8, Supplementary Fig. 1, Supplementary Tables 1–5 and Supplementary Videos 9 and 10) and C.E. (Fig. 5d, Extended Data Figs. 7 and 8 and Supplementary Fig. 4). I.G.D., Y.L., S.I., J.L. and C.E. interpreted the results, wrote and reviewed the manuscript and produced the figures. I.G.D. and J.L. managed and supervised the project and acquired funding.

Competing interests

The authors declare no competing interests.

Additional information

Extended data is available for this paper at https://doi.org/10.1038/s41564-021-00894-z.

Supplementary information The online version contains supplementary material available at https://doi.org/10.1038/s41564-021-00894-z.

Correspondence and requests for materials should be addressed to I.G.D.

Peer review information *Nature Microbiology* thanks Daniela Barilla, Joe Lutkenhaus, William Margolin and the other, anonymous, reviewer(s) for their contribution to the peer review of this work. Peer reviewer reports are available.

Reprints and permissions information is available at www.nature.com/reprints.

Publisher's note Springer Nature remains neutral with regard to jurisdictional claims in published maps and institutional affiliations.

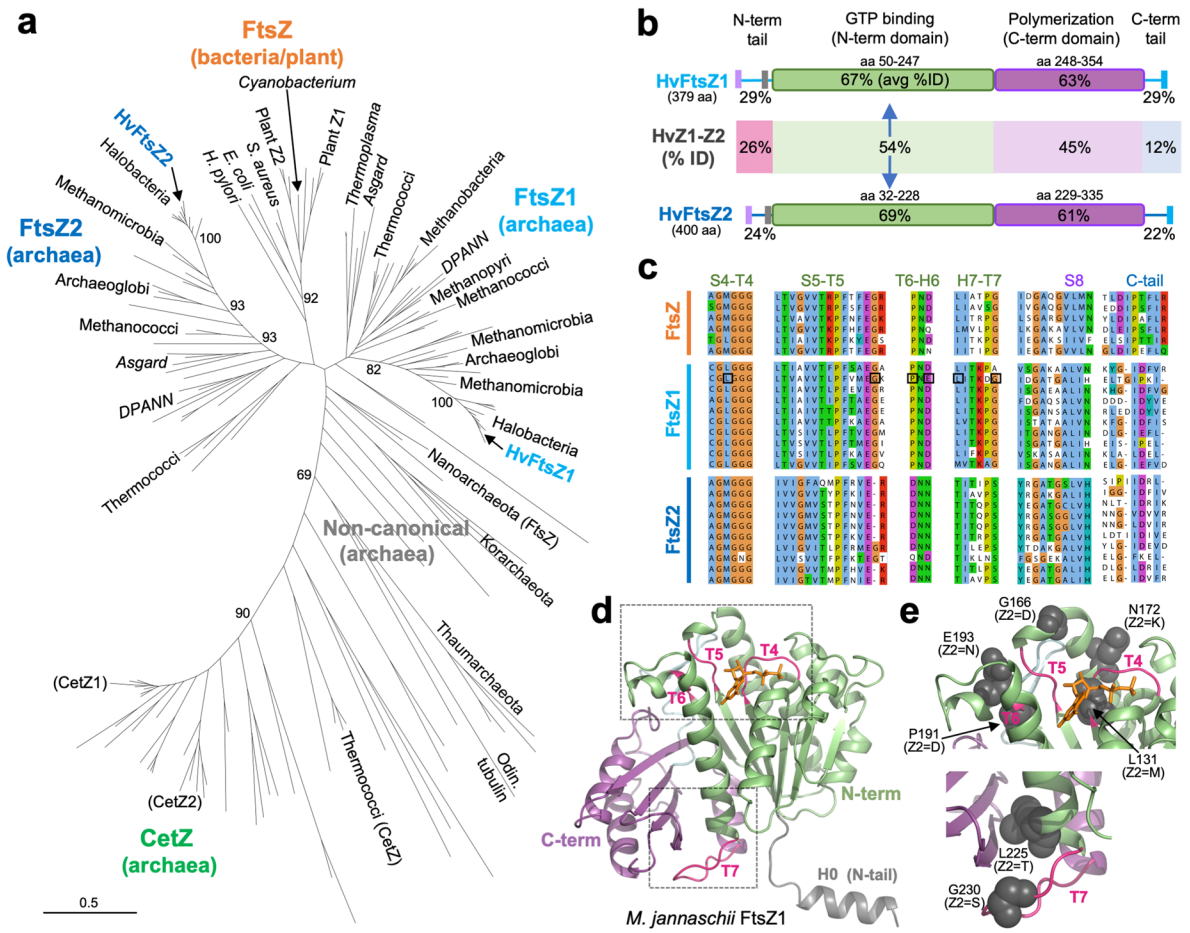

Extended Data Fig. 1 | Molecular phylogeny and comparison of archaeal FtsZ1 and FtsZ2 families. a, Maximum likelihood phylogenetic tree based on an alignment of the tubulin superfamily proteins identified in 60 diverse archaeal genomes (Supplementary Table 3), and the 13 bacterial and plant sequences used to identify them. Bootstrap support is shown for selected branches (%). **b**, Domain organization and percent sequence identities for FtsZ1 and FtsZ2. The percentages over the domains (green and purple boxes) indicate the average sequence identity in that region for each *H. volcanii* FtsZ compared to all of the other members of the same family that were identified in the Archaea domain. The region between FtsZ1 and FtsZ2 represents the percent identity in the region between the *H. volcanii* FtsZ1 and FtsZ2 (%ID). The approximate location of conserved sequence motifs within the tail regions are indicated by vertical bars, coloured to indicate similarities between the two. **c**, Aligned sequence regions containing conserved differences between the bacterial/plant FtsZ and the archaeal FtsZ1 and FtsZ2 families, labelled with the secondary structural elements. Boxed residues indicate conserved sites that are displayed in panel (**e**). **d**, Crystal structure of FtsZ1 from *Methanocaldococcus jannaschii* (PDB: 1FSZ), with selected loops (T4-T7) involved in nucleotide binding and hydrolysis shown in pink. GDP is shown in orange, and the main domains are coloured as in panel (**b**). Boxed regions are expanded in panel (**e**), which displays some conserved residues that characteristically differ between the FtsZ1 and FtsZ2 families (grey space-filling models, with FtsZ2 consensus residues in parentheses) and cluster around the nucleotide-dependent polymerization surfaces.

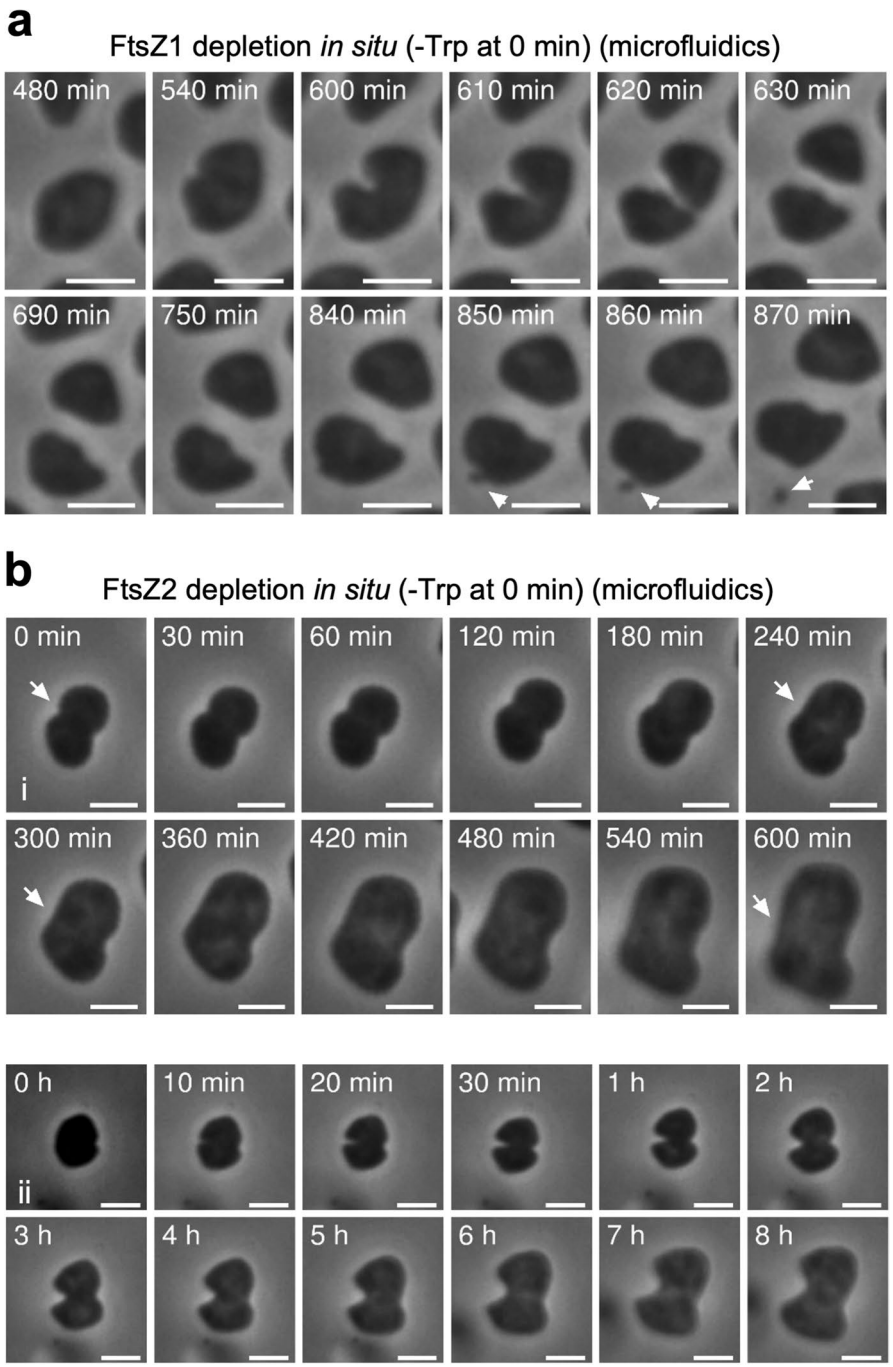

Extended Data Fig. 2 | Partial division phenotypes during depletion of FtsZ1 or FtsZ2. a, *H. volcanii* ID56 (*p.tna-ftsZ1*) was cultured in Hv-Cab + 2 mM Trp, and then loaded into a microfluidics platform and cultured with a flow of Hv-Cab (without Trp) over 15 h (0.5 p.s.i) to deplete FtsZ1. Shown is one cell that was identified to divide (unilaterally), even after ~9 h of depletion, and then one cell exhibited a budding-like process (arrows). Scale bars, 2 μm. **b**, *H. volcanii* ID57 (*p.tna-ftsZ2*) was pre-cultured in Hv-Cab + 2 mM Trp, and then loaded into a microfluidics platform and cultured with a flow of Hv-Cab + 2 mM Trp for 3 h, followed by Hv-Cab (no Trp) for 10 h (2 p.s.i) to deplete FtsZ2. The zero timepoint represents the start of medium flow without Trp. During the early stage of depletion of FtsZ2, partial constrictions were sometimes observed, as seen in these two examples (i and ii), but these never completed division and the constriction eventually reversed over several hours (see arrows). Cells, however, retained some apparent 'memory' of the initial constriction often manifesting as a somewhat bilobed shape. The data shown is representative of at least two independent experiments. Scale bars, 2 μm.

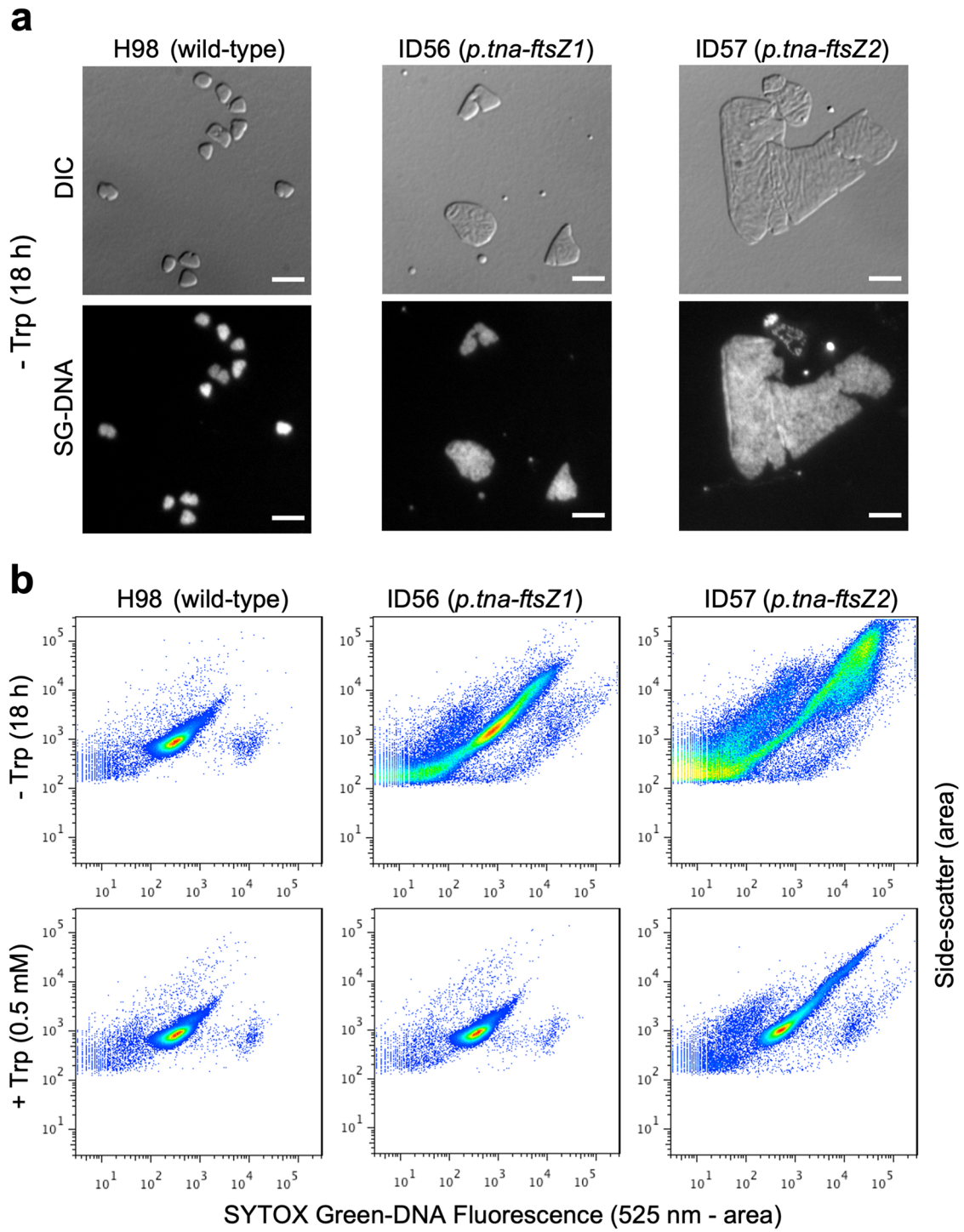

Extended Data Fig. 3 | Cellular DNA content during depletions of FtsZ1 and FtsZ2. a, SYTOX Green (SG) DNA staining of cells sampled from cultures 18 h after resuspension of mid-log cells in media without Trp. Stained cells were placed on an agarose pad and visualized by differential-interference contrast (DIC) and fluorescence microscopy (lower panels). Scale bars, 5 µm. **b**, Flow cytometry analyses of cells sampled as per panel (**a**) (upper three panels), displaying side-scatter (as a proxy for cell size) versus SYTOX Green (SG)-DNA fluorescence. The lower three panels represent cultures treated in the same way, except 0.5 mM Trp was included in the medium. The data shown is representative of at least two independent experiments. The individual datapoints represent the area under the curve of each event detected; events were detected by a threshold of the side-scatter signal. After 18 h of *ftsZ1* or *ftsZ2* depletion, many very large cells with correspondingly high DNA content were observed, consistent with the images shown in panel (**a**). This indicates that DNA synthesis continues in proportion to the increase in cell volume during inhibition of cell division caused by depletion of FtsZ1 or FtsZ2.

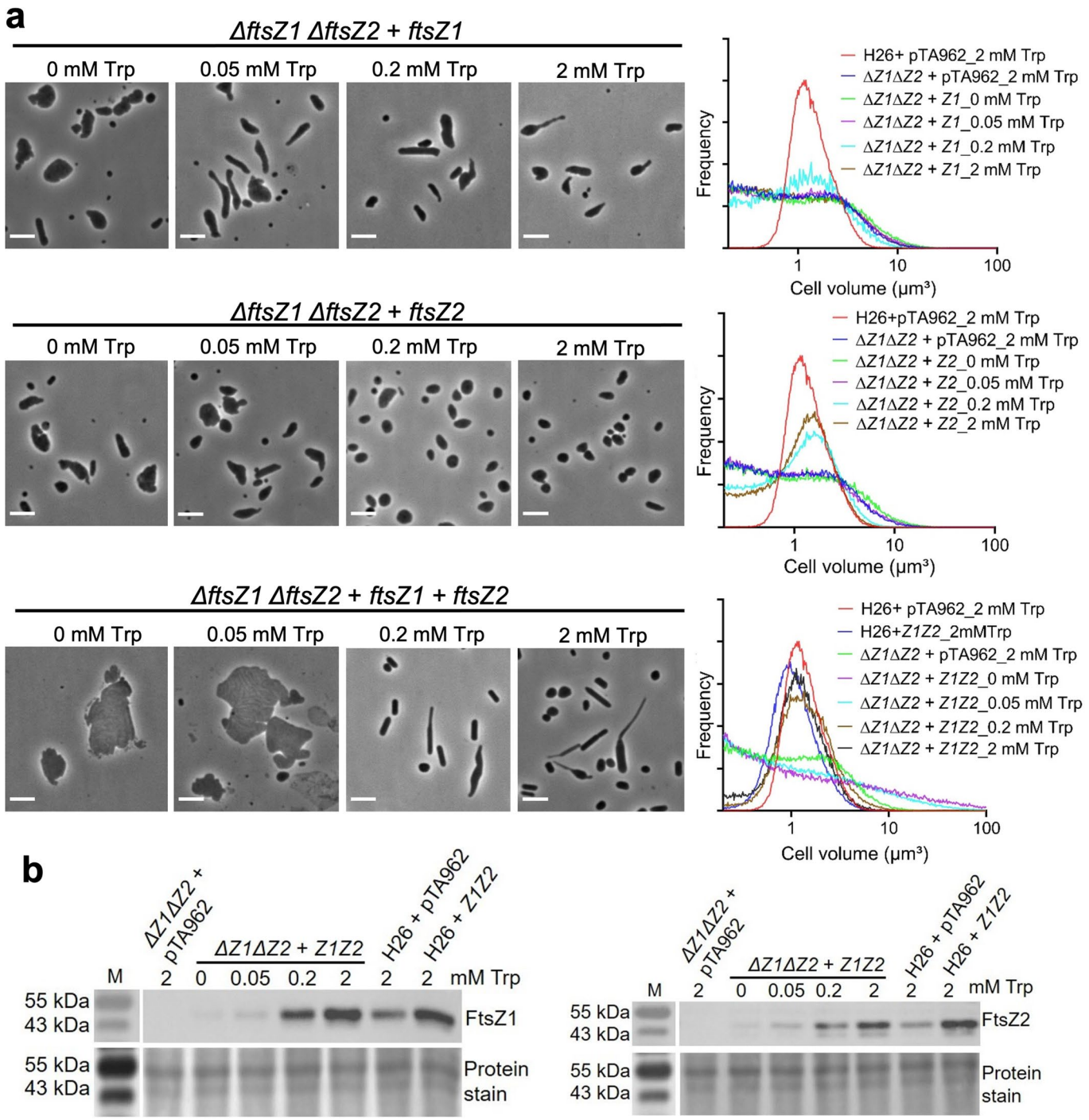

Extended Data Fig. 4 | Complementation of Δ*ftsZ1* Δ*ftsZ2*. a, Phase-contrast images (left) and Coulter cytometry (right) of strains based on *H. volcanii* ID112 (Δ*ftsZ1* Δ*ftsZ2*), plus pTA962-based plasmids expressing the indicated *ftsZ* genes, sampled during mid-log growth with the indicated concentrations of Trp. The same dataset for the wild-type control (H26 + pTA962) is shown in all graphs as a reference. Scale bars, 5 µm. **b**, Corresponding western blot analyses of FtsZ1 and FtsZ2 protein levels in total cell extracts of the indicated strains. The data shown is representative of two independent experiments.

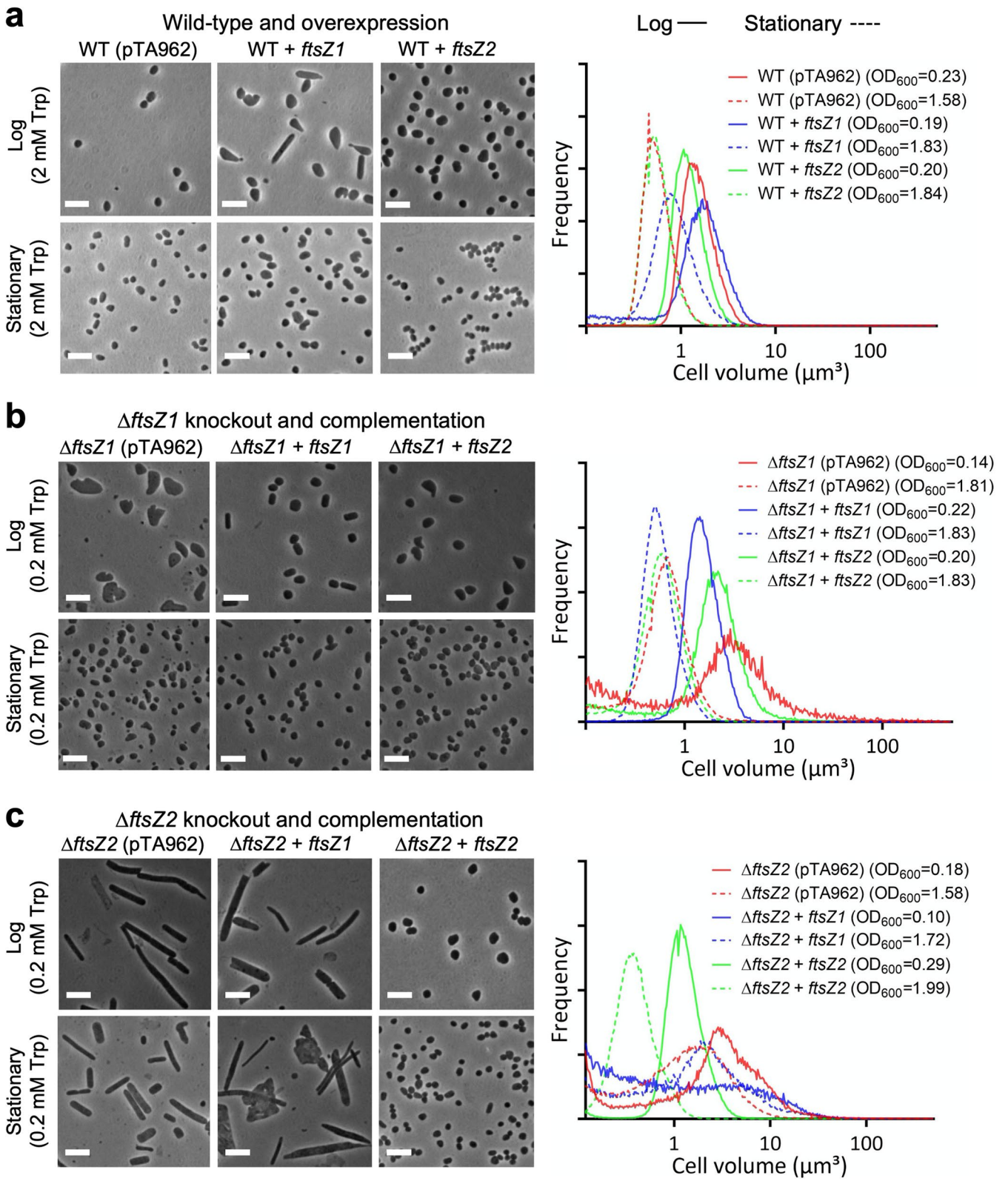

Extended Data Fig. 5 | See next page for caption.

Extended Data Fig. 5 | Comparison of *ftsZ* mutant cellular phenotypes in log and stationary phases. The differing functions of FtsZ1 and FtsZ2 were also apparent when cultures of the knock-out, complementation and overexpression strains were compared in mid-log and stationary phases. Phase-contrast images (left) and Coulter cytometry distributions (right) of the wild-type and overexpression strains (**a**) and the indicated *ftsZ* knockout and complementation strains **b, c**, all grown in Hv-Cab with the indicated concentration of Trp and sampled at mid-log and stationary phases. The data shown are representative of at least two independent experiments. Scale bars, 5 μm. Compared to mid-log cells, all the strains except the strains without a copy of *ftsZ2*, tended towards the wild-type size (smaller) and regular plate morphology in stationary phase. The Δ*ftsZ2* strains were somewhat smaller in stationary phase, but maintained greatly enlarged giant plate and elongated cells, suggesting a poor recovery as cell growth slows in stationary phase. These findings suggest that FtsZ2 confers a partial ability to divide and recover more normal cell sizes as the cell growth rate slows in stationary phase, whereas cells without FtsZ2 have a much stronger block to division that is maintained even as cells slow or stop growth in stationary phase.

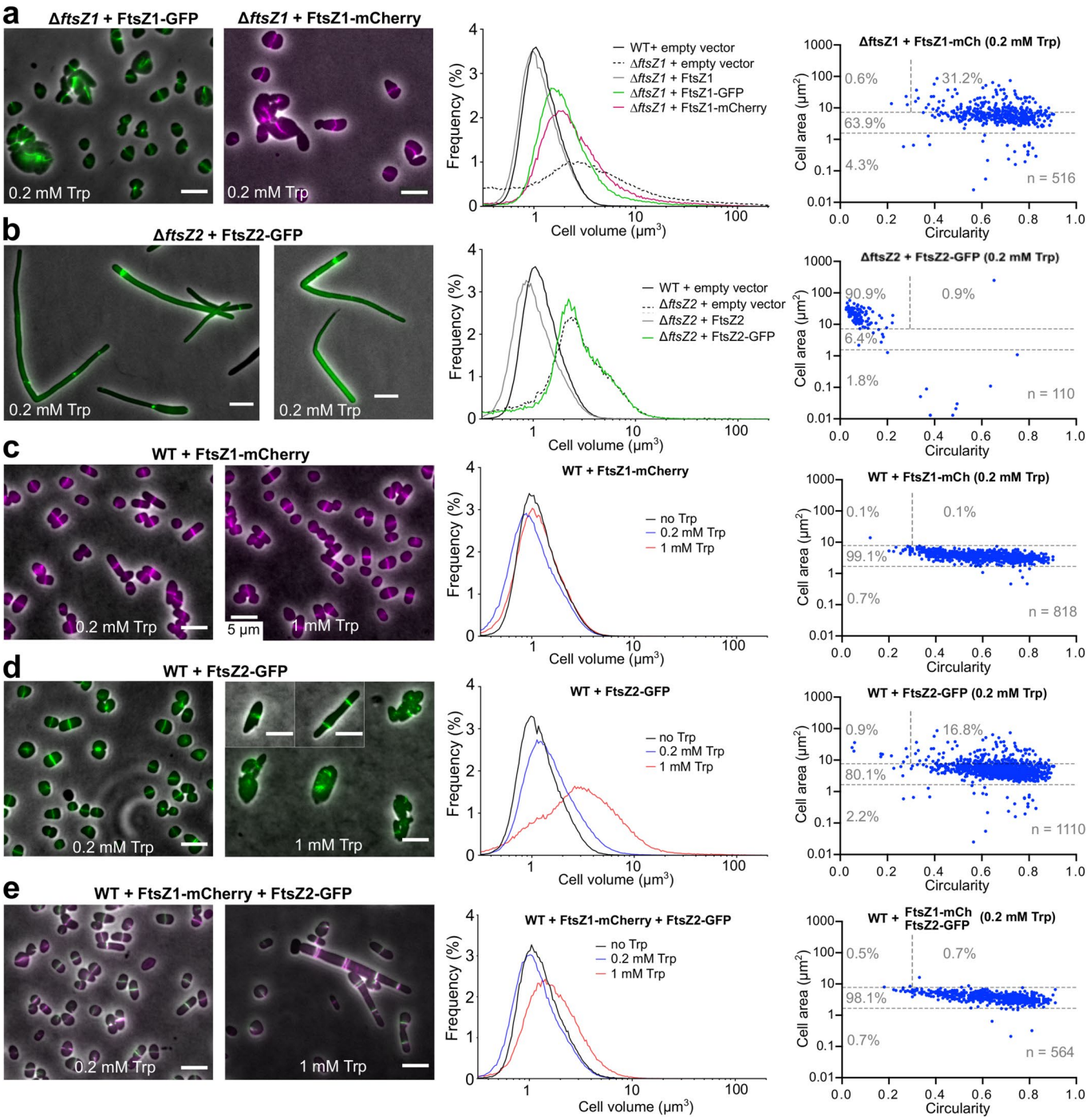

Extended Data Fig. 6 | FtsZ1 and FtsZ2 fluorescent fusions are not fully functional as sole copies but at moderate concentrations have minimal impact on cell division in the wild type. a-b, FtsZ1 and FtsZ2 fluorescent fusion proteins were functionally tested in their respective Δ*ftsZ1* or Δ*ftsZ2* backgrounds by phase-contrast and fluorescence microscopy (left) and by Coulter cytometry (right) for cell size. FtsZ1-GFP and FtsZ1-mCherry (0.2 mM Trp) partially complement Δ*ftsZ1*. **b**, FtsZ2-GFP was unable to complement the Δ*ftsZ2* background, whereas the untagged protein achieves full complementation (0.2 mM Trp). The same dataset for the wild-type control is shown in both graphs as a reference. **c-e**, When expressed in wild-type cells, FtsZ1-mCherry or FtsZ2-GFP, or both, cause minimal effects on cell size and shape at a moderate level of expression (0.2 mM Trp), and show sharp midcell bands. These proteins are therefore useful localization markers for division, although detailed analyses of FtsZ subcellular ultrastructure and dynamics await the development of functional complete labelling. The data shown are representative of at least two independent experiments. Scale bars, 5 μm.

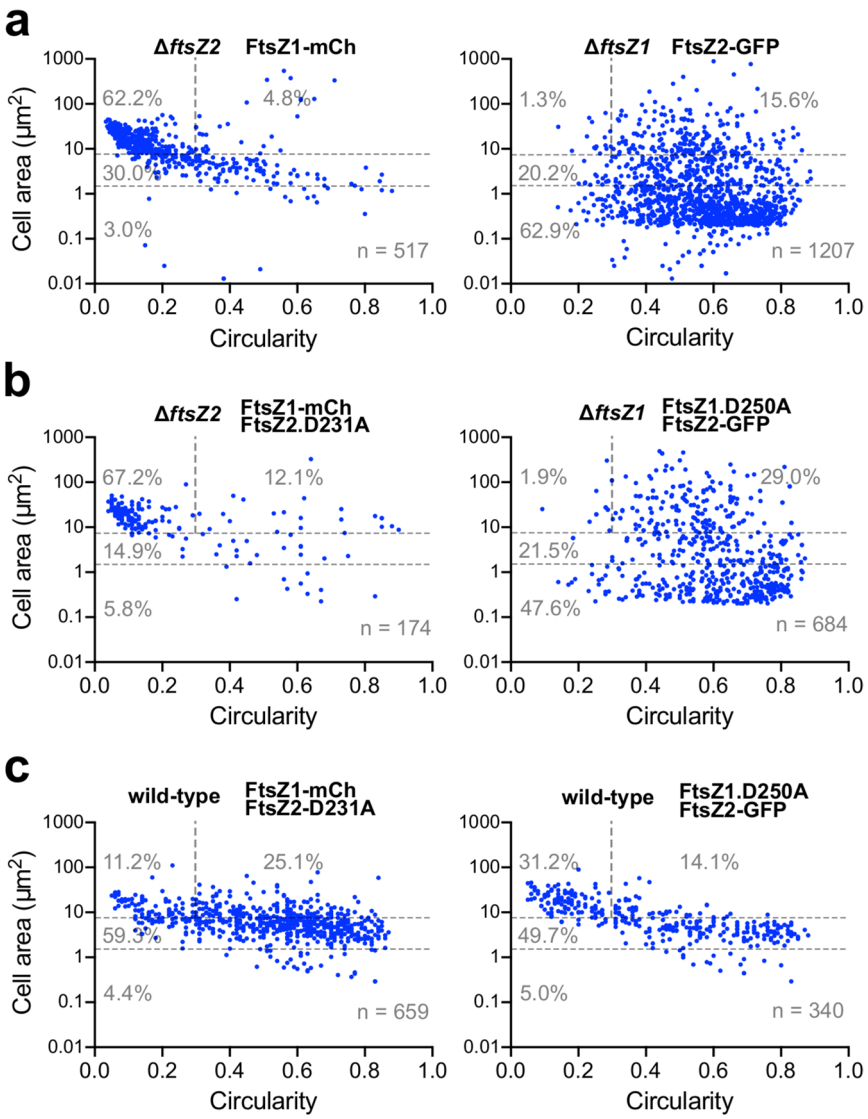

Extended Data Fig. 7 | Cell shape analyses for FtsZ localization interdependency studies. Cell area and shape (circularity) were determined for individual cells, as per Fig. 5 (0.2 mM Trp), and data were combined from two replicate experiments in for each plot. The plots are labelled with the strain's relevant genomic background (left) and the *ftsZ* variant(s) expressed on the plasmid (right). The data shown are representative of at least two independent experiments.

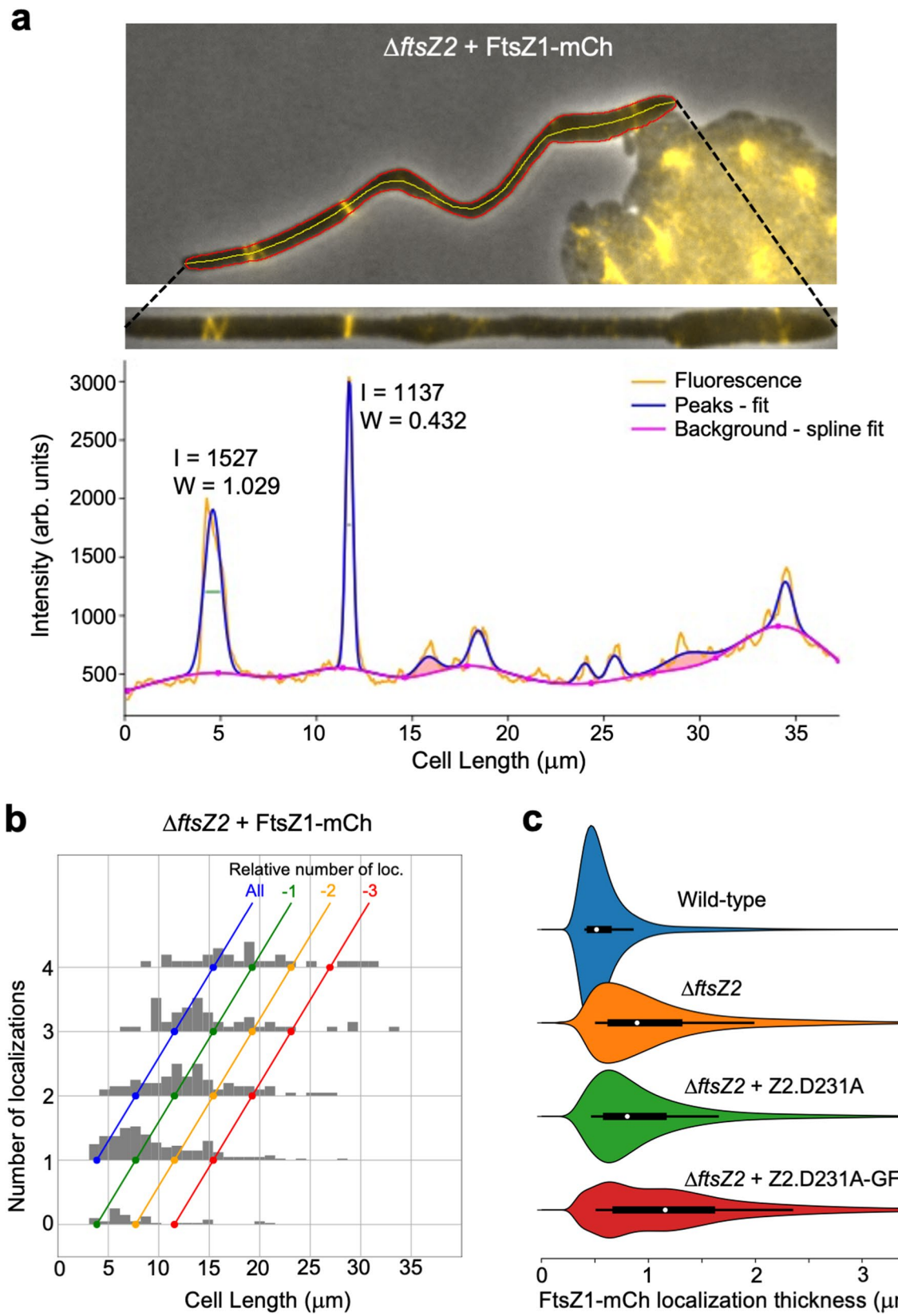

Extended Data Fig. 8 | See next page for caption.

Extended Data Fig. 8 | FtsZ1-mCh localization in *ftsZ2*-mutant strains. a, Demonstration of the automated image analysis procedure for determining FtsZ localization parameters. Cell outlines were obtained (red), and the fluorescence (FtsZ1-mCherry in yellow) was quantified by averaging the intensity on the transverse axis to create a longitudinal intensity profile. Gaussian peaks were fitted to the detected localizations and a spline fit to the background. The localization thickness (W) was taken as the width of the fitted Gaussian peaks at half height (μm), and the intensity (I) was taken as the integrated peak area (per μm across the cell). See *Methods* for further details. **b**, Histograms for cells with the indicated number of localizations *versus* cell length for Δ*ftsZ2* + FtsZ1-mCh. Colored lines indicate the lengths of cells that have the indicated relative number of localizations per unit length. **c**, Violin plots of the thickness of FtsZ1-mCh localization in the indicated strain backgrounds; the median is indicated by a white dot, the thick bar is the interquartile range, and thin bar is the 9th-91st percentile range. The data shown are representative of at least two independent experiments. Explanation of the experiment using the Δ*ftsZ2* + FtsZ2.D231A-GFP + FtsZ1-mCh strain is given in the Supplementary results and discussion and Extended Data Fig. 10.

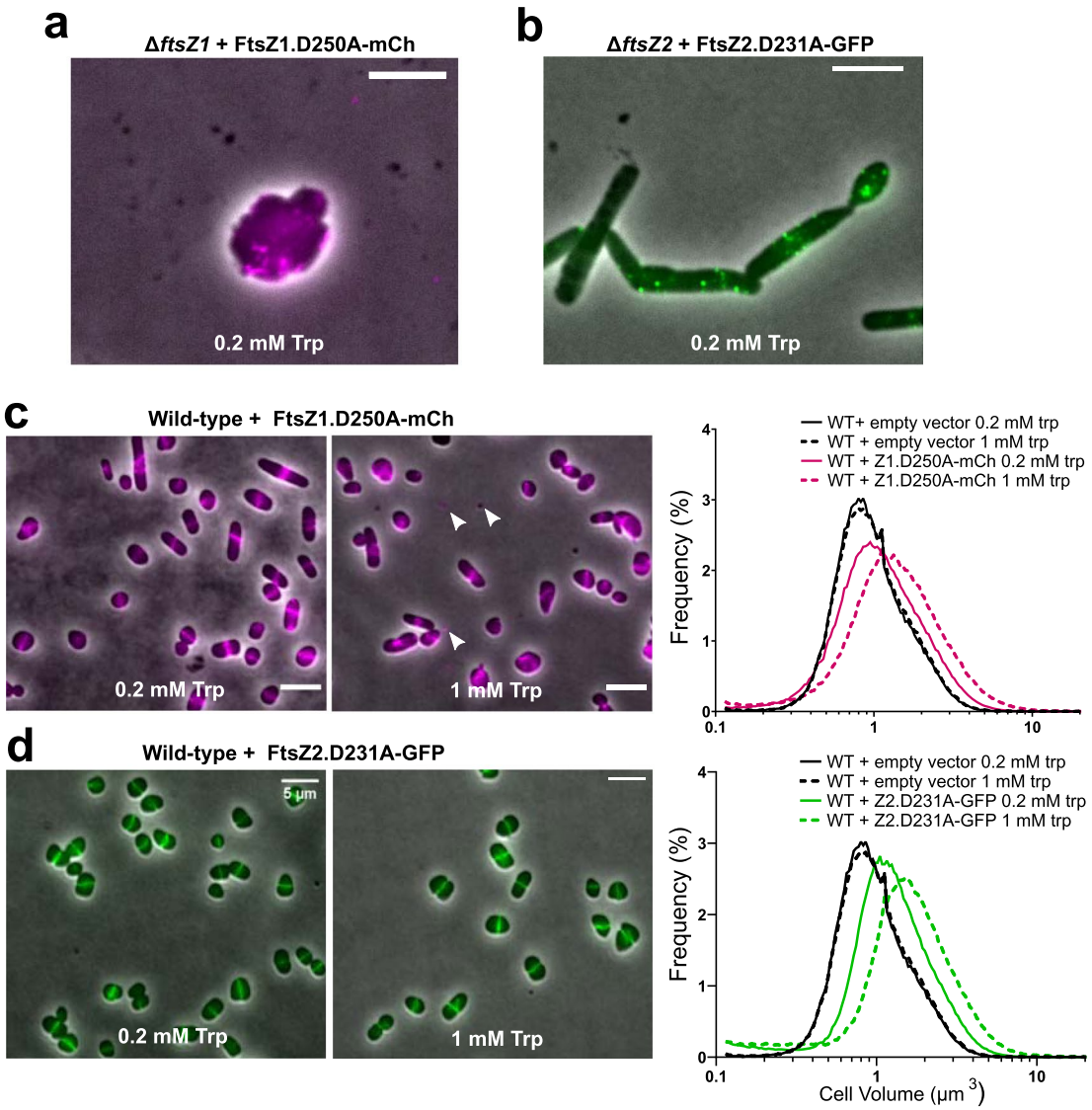

Extended Data Fig. 9 | Localization of FtsZ T7-loop mutants, *ftsZ1.D250A-mCh* and *ftsZ2.D231A-GFP*. a-b, The FP-tagged T7 mutants fail to complement their respective Δ*ftsZ* strain. **c-d**, Suppression of the severe dominant-inhibitory effects of the T7 mutants by the fluorescent tags, shown by phase-contrast and fluorescence microscopy (left) and Coulter cytometry (right). FtsZ1.D250A-mCh showed aberrant localization and cellular distortions and envelope protrusions associated with the fluorescent filaments; small fluorescent particles detatched from cells are also evident (arrowheads). Yet the cell size distribution was only subtly affected. The data shown are representative of at least two independent experiments. Similar results were obtained with FtsZ1.D250A-GFP (*H. volcanii* ID153). FtsZ2.D231A-GFP shows similar localization to wild-type (FtsZ2-GFP), with only a moderate increase in cell size increase observed at 1mM Trp; note that FtsZ2-GFP had a much stronger influence (Extended Data Fig. 6d). Scale bars, 5 µm.

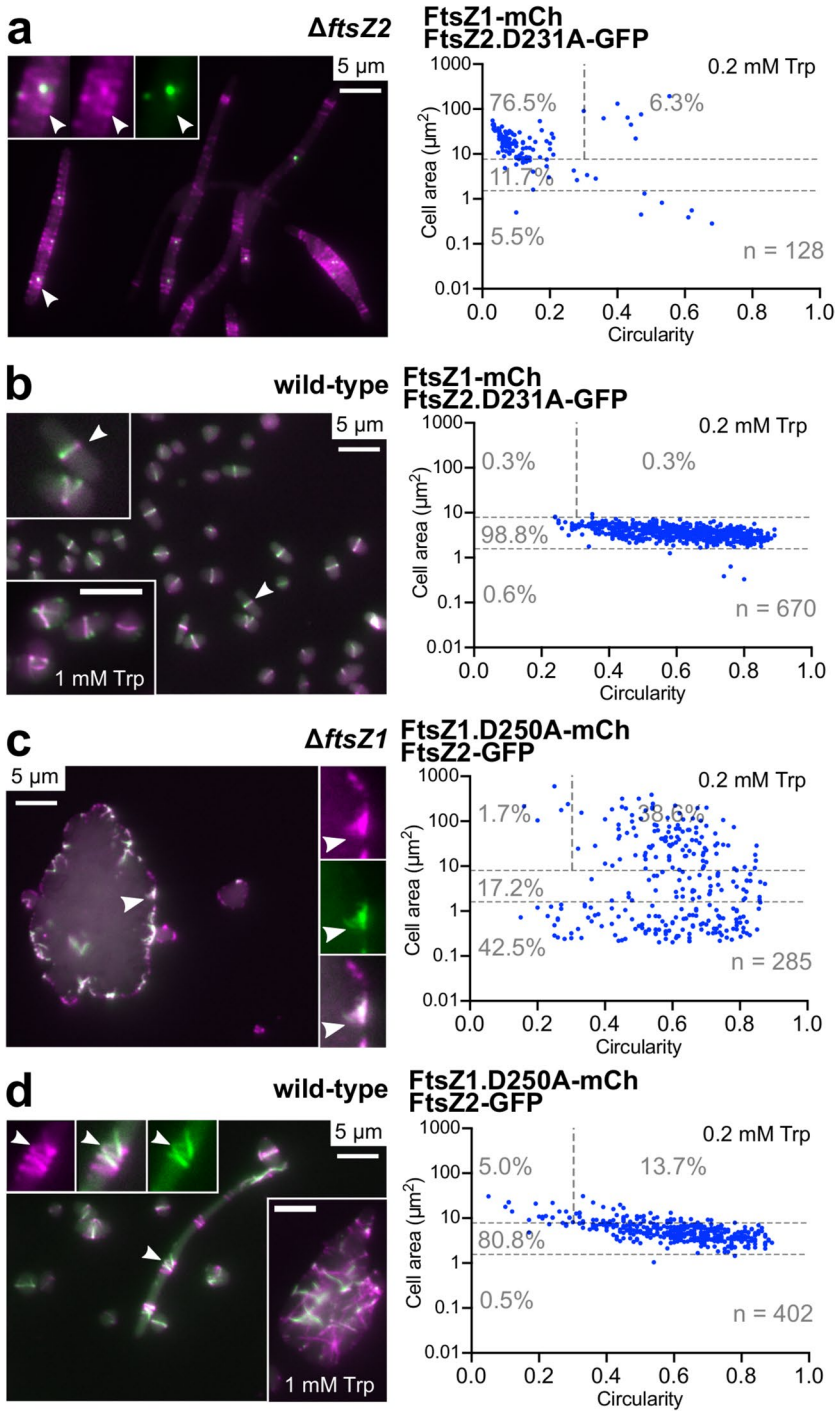

Extended Data Fig. 10 | Co-localization studies of wild-type FtsZ and T7-loop mutants. Fluorescence microscopy (overlay of GFP and mCherry channels; co-localization appears white) (left) and cell size/shape analysis plots (right) for the indicated strains (grown with 0.2 mM Trp) containing one tagged wild-type protein and the alternate tagged the T7-loop mutant. The data shown are representative of at least two independent experiments. In panels (**b**) and (**d**), results with cells grown with 1 mM Trp is shown in the lower insets; the morphology percentages for these were: (**b**) 95.4% wild-type-like, 3.2% giant plates, 0.9% filaments, and 0.5% debris (n = 439), and (**d**) 40.7% wild-type-like, 25.5% giant plates, 29.1% filaments, and 5.1% debris (n = 196). Scale bars, 5 μm.

nature research

Corresponding author(s): Iain G. Duggin

Last updated by author(s): Mar 9, 2021

Reporting Summary

Nature Research wishes to improve the reproducibility of the work that we publish. This form provides structure for consistency and transparency in reporting. For further information on Nature Research policies, see our Editorial Policies and the Editorial Policy Checklist.

Statistics

For all statistical analyses, confirm that the following items are present in the figure legend, table legend, main text, or Methods section.

n/a	Confirmed	
☐	☒	The exact sample size (*n*) for each experimental group/condition, given as a discrete number and unit of measurement
☐	☒	A statement on whether measurements were taken from distinct samples or whether the same sample was measured repeatedly
☒	☐	The statistical test(s) used AND whether they are one- or two-sided *Only common tests should be described solely by name; describe more complex techniques in the Methods section.*
☐	☒	A description of all covariates tested
☒	☐	A description of any assumptions or corrections, such as tests of normality and adjustment for multiple comparisons
☐	☒	A full description of the statistical parameters including central tendency (e.g. means) or other basic estimates (e.g. regression coefficient) AND variation (e.g. standard deviation) or associated estimates of uncertainty (e.g. confidence intervals)
☒	☐	For null hypothesis testing, the test statistic (e.g. *F*, *t*, *r*) with confidence intervals, effect sizes, degrees of freedom and *P* value noted *Give P values as exact values whenever suitable.*
☒	☐	For Bayesian analysis, information on the choice of priors and Markov chain Monte Carlo settings
☒	☐	For hierarchical and complex designs, identification of the appropriate level for tests and full reporting of outcomes
☒	☐	Estimates of effect sizes (e.g. Cohen's *d*, Pearson's *r*), indicating how they were calculated

Our web collection on statistics for biologists contains articles on many of the points above.

Software and code

Policy information about availability of computer code

Data collection	Commercial software with the specific versions of the instruments indicated in the Methods were used for data collection.
Data analysis	The following software packages were used for data analysis, where indicated in the Methods: FIJI (ver 2.1), MicrobeJ (ver 5.13), MEGA (ver 7.0.26), PyMol (ver. 1.7), MUSCLE (ver 1), Clustal X (ver 2), Jalview (ver 2), Nikon Nis-Elements (ver AR 4.60.00) for confocal data processing, and Bitplane scientific IMARIS (ver 7.6.4) for 3D-SIM data rendering.

For manuscripts utilizing custom algorithms or software that are central to the research but not yet described in published literature, software must be made available to editors and reviewers. We strongly encourage code deposition in a community repository (e.g. GitHub). See the Nature Research guidelines for submitting code & software for further information.

Data

Policy information about availability of data

All manuscripts must include a data availability statement. This statement should provide the following information, where applicable:

- Accession codes, unique identifiers, or web links for publicly available datasets
- A list of figures that have associated raw data
- A description of any restrictions on data availability

Source data files for the Figures, Extended Data Figures, and Supplementary Figures, including graphs, raw western blot images and the phylogenetic tree, are available with the online version of this article. Other data and biological materials are available from the corresponding author upon reasonable request. The NCBI (www.ncbi.nlm.nih.gov/protein/) and Uniprot (www.uniprot.org) protein sequence databases were searched to obtain sequences of archaeal tubulin superfamily proteins. Genome sequence data generated in this study has been deposited at NCBI under BioProject PRJNA681931.

Field-specific reporting

Please select the one below that is the best fit for your research. If you are not sure, read the appropriate sections before making your selection.

☒ Life sciences ☐ Behavioural & social sciences ☐ Ecological, evolutionary & environmental sciences

For a reference copy of the document with all sections, see nature.com/documents/nr-reporting-summary-flat.pdf

Life sciences study design

All studies must disclose on these points even when the disclosure is negative.

Sample size	Samples size was determined by the practical maximum capacity of the instrument to record data for individual cells at random. For the Coulter and Flow cytometry methods described, 30,000 - 100,000 events per sample were normally recorded.
Data exclusions	No data exclusions were applied.
Replication	In addition to preliminary experiments carried out throughout this study, the data displayed are representative of or pooled from at least two separate replicate experiments as indicated in the figure legends, all of which showed consistent outcomes. The representative data, microscopy images and accompanying descriptions we chosen to fairly represent the whole experimental datasets.
Randomization	Cell samples were randomized by sampling liquid suspension cultures and by the analytical instruments used in the study.
Blinding	Most sample identities were not blinded to the investigators owing to costs and impracticalities. Individual cells were selected at random by analytical instruments (e.g. cytometers), and such sampling was thus blinded from the investigators. Microscopy fields of view were not blinded, and they were only assessed during acquisition to the extent that they contained cells. All such fields of view were subjected to the image analyses described in the Methods.

Reporting for specific materials, systems and methods

We require information from authors about some types of materials, experimental systems and methods used in many studies. Here, indicate whether each material, system or method listed is relevant to your study. If you are not sure if a list item applies to your research, read the appropriate section before selecting a response.

Materials & experimental systems

n/a	Involved in the study
☐	☒ Antibodies
☒	☐ Eukaryotic cell lines
☒	☐ Palaeontology and archaeology
☒	☐ Animals and other organisms
☒	☐ Human research participants
☒	☐ Clinical data
☒	☐ Dual use research of concern

Methods

n/a	Involved in the study
☒	☐ ChIP-seq
☐	☒ Flow cytometry
☒	☐ MRI-based neuroimaging

Antibodies

Antibodies used	Polyclonal serum against custom peptides derived from the sequence of FtsZ1 (Cambridge Research Biochemicals, UK) and FtsZ2 (Thermo-Fischer, USA). A donkey anti-rabbit IgG-HRP (AbCam 16284) was used as the secondary antibody for westerns at a dilution of 1:5000.
Validation	Antisera against FtsZ1 and FtsZ2 were tested at a range of concentrations in Western blots, probing the total cell extracts from WT and the two FtsZ-deletion strains. This verified the specificity of detection of proteins of approximately the expected size (by SDS-PAGE) only in the wild-type cell extract.

Flow Cytometry

Plots

Confirm that:

☒ The axis labels state the marker and fluorochrome used (e.g. CD4-FITC).

☒ The axis scales are clearly visible. Include numbers along axes only for bottom left plot of group (a 'group' is an analysis of identical markers).

☒ All plots are contour plots with outliers or pseudocolor plots.

☒ A numerical value for number of cells or percentage (with statistics) is provided.

Methodology

Sample preparation	Cell samples were randomized by sampling liquid suspension cultures, grown as described in the Methods.
Instrument	BD LSR-II analytical flow cytometer
Software	BD FACSDiva (ver 6).
Cell population abundance	Analytical flow cytometry was performed, in which 30,000 to 100,000 events were recorded for random cells.
Gating strategy	No gating applied. Event detection was triggered with a side-scatter threshold.

☐ Tick this box to confirm that a figure exemplifying the gating strategy is provided in the Supplementary Information.